Initiation of large-volume silicic centers in the Yellowstone hotspot track: insights from H2O- and F-rich quartz-hosted rhyolitic melt inclusions in the Arbon Valley Tuff of the S...

ARTICLE *in* CONTRIBUTIONS TO MINERALOGY AND PETROLOGY · JANUARY 2016

Impact Factor: 3.48 · DOI: 10.1007/s00410-015-1210-z

4 AUTHORS, INCLUDING:

Dana Drew

University of Oregon

3 PUBLICATIONS **14** CITATIONS

SEE PROFILE

Ilya Bindeman

University of Oregon

175 PUBLICATIONS **3,108** CITATIONS

SEE PROFILE

Matthew W. Loewen

University of Oregon

10 PUBLICATIONS **21** CITATIONS

SEE PROFILE

Contrib Mineral Petrol (2016) 171:10
DOI 10.1007/s00410-015-1210-z

ORIGINAL PAPER

Initiation of large-volume silicic centers in the Yellowstone hotspot track: insights from H_2O- and F-rich quartz-hosted rhyolitic melt inclusions in the Arbon Valley Tuff of the Snake River Plain

Dana L. Drew[1,2] · Ilya N. Bindeman[1] · Matthew W. Loewen[1] · Paul J. Wallace[1]

Received: 8 February 2015 / Accepted: 12 November 2015

Abstract During the onset of caldera cluster volcanism at a new location in the Snake River Plain (SRP), there is an increase in basalt fluxing into the crust and diverse silicic volcanic products are generated. The SRP contains abundant and compositionally diverse hot, dry, and often low-$\delta^{18}O$ silicic volcanic rocks produced through time during the formation of individual caldera clusters, but more H_2O-rich eruptive products are rare. We report analyses of quartz-hosted melt inclusions from pumice clasts from the upper and lower Arbon Valley Tuff (AVT) to gain insight into the initiation of caldera cluster volcanism. The AVT, a voluminous, caldera-forming rhyolite, represents the commencement of volcanism (10.44 Ma) at the Picabo volcanic field of the Yellowstone hotspot track. This is a normal $\delta^{18}O$ rhyolite consisting of early and late erupted members (lower and upper AVT, respectively) with extremely radiogenic Sr isotopes and unradiogenic Nd isotopes, requiring that ~50 % of the mass of these elements is derived from melts of Archean upper crust. Our data reveal distinctive features of the early erupted lower AVT melt including: variable F concentrations up to 1.4 wt%, homogenous and low Cl concentrations (~0.08 wt%), H_2O contents ranging from 2.3 to 6.4 wt%, CO_2 contents ranging from 79 to 410 ppm, and enrichment of incompatible elements compared to the late erupted AVT, subsequent Picabo rhyolites, SRP rhyolites, and melt inclusions from other metaluminous rhyolites (e.g., Bishop Tuff, Mesa Falls Tuff). We couple melt inclusion data with Ti measurements and cathodoluminescence (CL) imaging of the host quartz phenocrysts to elucidate the petrogenetic evolution of the AVT rhyolitic magma. We observe complex and multistage CL zoning patterns, the most critical being multiple truncations indicative of several dissolution–reprecipitation episodes with bright CL cores (higher Ti) and occasional bright CL rims (higher Ti). We interpret the high H_2O, F, F/Cl, and incompatible trace element concentrations in the context of a model involving melting of Archean crust and mixing of the crustal melt with basaltic differentiates, followed by multiple stages of fractional crystallization, remelting, and melt extraction. This multistage process, which we refer to as distillation, is further supported by the complex CL zoning patterns in quartz. We interpret new $\Delta^{18}O$(Qz-Mt) isotope measurements, demonstrating a 0.4 ‰ or ~180 °C temperature difference, and strong Sr isotopic and chemical differences between the upper and lower AVT to represent two separate eruptions. Similarities between the AVT and the first caldera-forming eruptions of other caldera clusters in the SRP (Yellowstone, Heise and Bruneau Jarbidge) suggest that the more evolved, lower-temperature, more H_2O-rich rhyolites of the SRP are important in the initiation of a caldera cluster during the onset of plume impingement.

Keywords Arbon Valley Tuff · Picabo · Snake River Plain · Caldera · Rhyolite · Melt inclusion

Communicated by Timothy L. Grove.

Electronic supplementary material The online version of this article (doi:10.1007/s00410-015-1210-z) contains supplementary material, which is available to authorized users.

✉ Dana L. Drew
ddrew@utexas.edu

[1] Department of Geological Sciences, University of Oregon, Eugene, OR, USA

[2] Present Address: Department of Geological Sciences, University of Texas, Austin, TX, USA

Published online: 07 January 2016

Introduction

Snake River Plain silicic volcanism and caldera cycles

The Yellowstone hotspot track has recorded a comprehensive 16 million year history of voluminous silicic volcanism and preserved a series of caldera clusters and eruptive centers throughout the Snake River Plain (SRP). The volcanic fields we discuss from east to west include the Yellowstone Plateau, Heise, Picabo, Twin Falls, and Bruneau Jarbidge (Fig. 1). These volcanic fields represent a conveyor belt-like, spatially and temporally separated, record of volcanism. An abundance of hot, dry, nearly aphyric, and densely welded rhyolites are observed and considered characteristic of these volcanic fields and of rhyolite genesis along the Yellowstone hotspot track (Williams 1941; Branney et al. 2008; Bonnichsen et al. 2008; Ellis et al. 2013). However, less common crystal-rich and less densely welded rhyolites are also associated with many of the volcanic fields in the SRP, including Picabo, Bruneau Jarbidge, Heise and Yellowstone; these have been interpreted to be more H_2O-rich and to have lower pre-eruptive temperatures (Nash et al. 2006).

Almeev et al. (2012) demonstrated based on phase relations that the Bruneau Jarbidge rhyolite can contain as little as 1–0.6 wt% H_2O, yet biotite- and amphibole-bearing SRP units can reach up to 4.8 and 2.9 wt% water, accordingly. This large range of water contents has implications for how we view rhyolite formation in the SRP. Recent work on rhyolite generation has also demonstrated that there are a variety of petrogenetic and thermomechanical mechanisms for magma genesis in different tectonic environments, resulting in rhyolites that range from crystal-rich and near solidus to crystal-poor and near liquidus (e.g., Dufek and Bachman 2010; Simakin and Bindeman 2012; Brueseke et al. 2014). In this paper, we focus on the generation of the first-erupted rhyolites from the Picabo volcanic center in the SRP and their implications for caldera cluster initiation.

Rhyolitic volcanism in the eastern SRP and extending into the western SRP is predominantly multicyclic, with calderas forming repeatedly at each location. Recent work (Watts et al. 2011; Bindeman et al. 2007; Drew et al. 2013) has

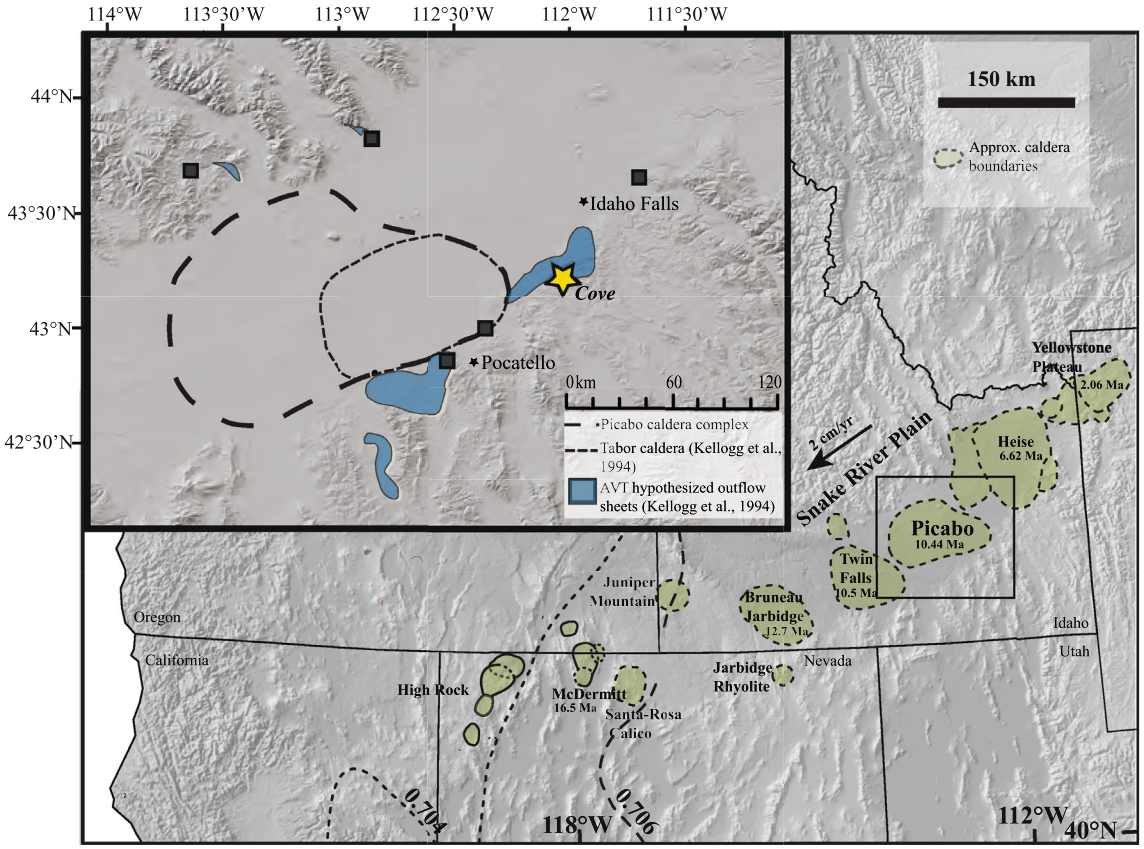

Fig. 1 Map of the Yellowstone hotspot volcanic fields and inset map of the AVT caldera (Drew et al. 2013) and Picabo caldera complex (modified from Drew et al. 2013), observed localities of the Arbon Valley Tuff (*dark gray squares*) at the Picabo volcanic field (modified from Drew et al. 2013). The *yellow star* is the Cove locality, where the samples for this study were collected. Juniper Mountain and Jarbidge Rhyolite locations are from Colón et al. (2015a)

demonstrated that these eruptive cycles in the eastern SRP begin with the eruption of normal-$\delta^{18}O$ rhyolites and end with the eruption of low $\delta^{18}O$ (<5.6 ‰) rhyolites with diverse $\delta^{18}O$ in zircons and occasionally quartz. In particular, rhyolites of the eastern SRP (Heise, Yellowstone, and Picabo) display these signatures due to the progressive recycling of volcanic products affected by hydrothermal alteration. In the western SRP, an overabundance of low-$\delta^{18}O$ magmas is observed in the Picabo, Twin Falls, and Bruneau–Jarbidge centers, and the exact temporal isotopic relations are less certain. Boroughs et al. (2005, 2012) and Ellis et al. (2013) favor contribution of a preexisting low-$\delta^{18}O$ source, while Drew et al. (2013) suggests the facilitation of Basin and Range extensional tectonics to accelerate the recycling of hydrothermally altered volcanic products (dates of extension confirmed by Konstantinou et al. 2012). Colón et al. (2015a, b) also suggest that the heat of the Columbia River Basalts could have allowed deep hydrothermal alteration in the western SRP, providing an alternate mechanism to caldera collapse for incorporation of low-$\delta^{18}O$ material into magmas.

Improved geochronological work has made the eruptive cycles increasingly well constrained at each volcanic center (Watts et al. 2011; Drew et al. 2013; Bindeman et al. 2007; Ellis et al. 2010; Cathey et al. 2008; Bonnichsen et al. 2008; Anders et al. 2014); however, the process of initiating volcanism at a new location remains a matter of contention. Early rhyolites such as the Arbon Valley Tuff (AVT) of the Picabo volcanic field (10.44–6.6 Ma) that represent the commencement of volcanism at each caldera cycle are largely buried by subsequent magmatism making their origin more enigmatic. The data of Anders et al. (2014), as well as Nash et al. (2006), support the interpretation that the AVT and other "ahead of the plume" volcanic units are features of low-degree mantle melting, whereas other researchers (Christiansen and McCurry 2008) consider these rhyolites to be related to Basin and Range extension. However, the on-axis location of the AVT deposit and presumed caldera (Anders et al. 2009, 2014; Kellogg et al. 1994), large AVT volume typical of other SRP centers, and occurrence of this massive ignimbrite on the northern and southern extents of the plain support the alternative view that the AVT is SRP-related. Drew et al. (2013) demonstrated the spatio-temporal association of the AVT with Picabo-related rhyolites, which supports the interpretation that the AVT (and other similar more hydrous and trace element-rich rhyolites) is an important aspect of SRP volcanism. We contend that the AVT represents a critical component of the initiation of rhyolitic volcanism at a new location and that such rhyolite generation would be facilitated by a ramping up magmatic input during the onset of plume impingement, followed by interaction of the mantle melts with previously melted and hybridized Archean crust. Interestingly, similar patterns are observed in the earliest ~31 Ma manifestation of the Yellowstone plume beneath Oregon, with the exception that previously erupted rhyolites are being cannibalized there (Seligman et al. 2014).

Defining chemical characteristics of early rhyolites of caldera cycles and the AVT

The AVT is biotite bearing, and chemically and isotopically zoned. The zoned tuff consists of two main parts: the lower tuff including the fallout tuff (PC-12; Drew et al. 2013) and the upper tuff (PC-14). Furthermore, the distinct isotopic characteristics of the AVT include normal to high $\delta^{18}O_{melt}$ (7.9–8.3 ‰), extremely radiogenic and zoned $^{87}Sr/^{86}Sr_i$ ratios (ranging from 0.72520 to 0.71488), and extremely low ε_{Nd} and ε_{Hf} ratios (−18 and −28, respectively, in the upper tuff; Drew et al. 2013). Isotopic mixing models by Drew et al. (2013) suggest that greater than 50 %, by mass, of the AVT was derived from melting of Archean upper crust. Such high proportions require an equal or larger amount of isotopically normal (mantle-like) basalt to melt the crust. The proportions of crust and mantle provide constraints on the processes and sources creating the volatile and trace element budget of the AVT.

Many of the first (or early), geochemically enriched rhyolites of SRP volcanic centers are the most crystal-rich (up to ~35 %) tuffs of their corresponding volcanic sequences and show elevated concentrations of F, Li, B, Rb, Nb, Y, Sn, Th, and U consistent with heightened levels of fractional crystallization and crustal melting (Watts et al. 2011; Hildreth et al. 1991; Nash et al. 2006; Drew et al. 2013). Along with the AVT (Fig. 1), we interpret the Huckleberry Ridge Tuff-Member C of Yellowstone, the Blacktail Creek Tuff of Heise, and the Jarbidge rhyolite of Bruneau Jarbidge ($\delta^{18}O = 8.8$, $\varepsilon_{Nd} = -23$; Colón et al. 2015a), to share these characteristics.

The more "crustal" radiogenic isotopic signatures (Sr, Nd, Hf) requiring large, ca 50 %, proportions of remelted Archean crust, normal to high $\delta^{18}O$, and enriched incompatible trace element signature of the AVT suggest that rhyolite generation involved a greater crustal component and lacks the characteristic low-$\delta^{18}O$ signature that is prevalent throughout the SRP (Bindeman et al. 2007; Watts et al. 2011, 2012). Although many chemical and isotopic characteristics of the AVT are atypical of SRP rhyolites, they are similar to many metaluminous rhyolites and A-type granites (e.g., Bishop Tuff; Hildreth et al. 1984) and metaluminous to slightly peraluminous topaz rhyolites (Christiansen et al. 1984, 1986, 2007). In this study, we investigate how the first large rhyolitic magma body of a caldera cluster was generated and assembled in the Archean crust in a ramp-up of increasing basaltic input caused by plume impingement (Fig. 1).

Goals of the present study

This study addresses the following questions:

1. How can the initiation of volcanism at a new caldera cluster produce rhyolite with a more enriched incompatible element signature in comparison with typical recycled, hot, dry, crystal-poor, and commonly low $\delta^{18}O$ rhyolites in the SRP?
2. What combination of source characteristics and formation processes causes high volatile contents in the AVT (inferred from lower pre-eruptive temperatures and confirmed by our new melt inclusion data)? These might include low degrees of mantle melting, repeated crustal melting and melt extraction throughout the upper crust to concentrate volatiles, but could also involve source rocks with unusually high volatile contents.
3. Does the chemically and isotopically zoned AVT represent a single eruption from a zoned magma chamber, coeval eruptions from different adjacent magma bodies, or separate eruptions closely spaced in time?

Methods

The presence of rapidly quenched pumice clasts, which are rare in the SRP, provides the unique opportunity to investigate pre-eruptive volatile content. Thus, we present pre-eruptive volatile and major and trace element data from quartz-hosted rhyolitic melt inclusions from the rapidly quenched fallout pumice that is a part of the lower AVT (whole-rock $SiO_2 = 76.9$ wt%). Quartz phenocrysts containing melt inclusions were extracted from individual pumice clasts. The melt inclusions that we analyzed were glassy and fully enclosed in the phenocryst host, and only rarely contained vapor bubbles (Appendix Fig. 12 a through e). Eighteen melt inclusions from the lower tuff (PC-12) were doubly intersected and analyzed for H_2O and CO_2 contents by Fourier transform infrared (FTIR) spectroscopy at the University of Oregon using a Thermo-Nicolet Nexus 670 FTIR spectrometer coupled with a Continuum IR microscope. When H_2O contents were too high to quantify using the fundamental OH stretching vibration at 3570 cm^{-1}, the 4520 cm^{-1} and 5230 cm^{-1} peaks, and the total water calculation by Zhang et al. (1997) were used (Appendix Table 2). Five inclusions were excluded from the final dataset because of noisy spectra due to small inclusion size that results in highly variable hydroxyl to molecular H_2O ratios for replicate spectra from individual melt inclusions (Appendix Table 3). In addition, 19 melt inclusions in pumice clasts from the upper AVT were singly intersected and polished.

Major elements and F, S, and Cl concentrations in melt inclusions from the upper and lower AVT were analyzed using a Cameca SX100 electron microprobe at the University of Oregon MicroAnalytical Facility (Appendix Table 4a, b) using a 15-kV accelerating voltage and a 10-μm beam size. To account for the effects of alkali migration, time-dependent intensity corrections were made for Na, K, Al, and Si. A 10-nA current was used for Na, Si, K, Al, Mg, Fe, and Ca, after which a 50-nA current was used for S, Cl, Ti, P, and F acquisition.

Zoning patterns in the 16 host quartz grains were imaged using cathodoluminescence (CL) with a FEI Quanta 200 environmental scanning electron microscope (ESEM) at the University of Oregon. Only portions of the quartz crystals are preserved through the melt inclusion preparation process, and therefore, additional quartz phenocrysts from the lower fallout and upper welded tuff of the AVT were CL imaged (Appendix Figs. 13 through 16). Trace elements Ti, Fe, K, Na, and Al in the host quartz phenocrysts were also determined on the Cameca SX100 electron microprobe using similar settings but a higher current of 100 nA and longer count times of 400 s on and off peak (Appendix Tables 7 and 8). The detection limit for Ti was 30 ppm, and therefore, no trends in quartz Ti concentrations were interpreted for measurements less than 30 ppm.

Trace elements of select melt inclusions from the lower tuff (PC-P3.3, PC-P2.2, PC-P2.6, PC-P3.1-1 and 2, PC-P6.3-1, PC-P5.1-1 and 2, PC-P1.4, PC-P1.2-1 and 2) and interstitial glass from the upper and lower tuff (samples PC-12, PC-14 and PC-76) were analyzed at Oregon State University in the W. M. Keck Collaboratory for Plasma Mass Spectrometry using a Photon Machines Analyte G2 193-nm ArF "fast" Excimer Laser with a 5- to 7-Hz pulse rate and a 50- to 85-μm spot size coupled with a Thermoscientific X Series 2 Quadrupole Mass Spectrometer. GSE-1G was used as a calibration standard, and Si concentrations determined in melt inclusions by electron microprobe were used as an internal standard for each analysis (Appendix Table 5). NIST-612, BCR-2G, and BHVO-2G were monitored as secondary standards to verify overall accuracy. For NIST-612, the accuracy was better than 10 % for all reported elements. Data reduction strategy and other instrument parameters can be found in Loewen and Kent (2012).

In order to measure quartz–magnetite oxygen isotopic temperature, reflecting quenched pre-eruptive conditions (e.g., Bindeman and Valley 2002), magnetite and quartz were extracted from individual pumice of the airfall and in the upper tuff (samples PC-12 and PC-14, respectively) and measured for $\delta^{18}O$ by laser fluorination IRMS at the University of Oregon [method described by Bindeman (2008)].

Results

Stratigraphy of the studied section

The AVT is considered a caldera-forming unit of the Picabo volcanic field, and it is observed on both the northern and

southern extents of the SRP, including correlation with the southern Hawley Springs Tuff (Kellogg et al. 1994; Drew et al. 2013; Fig. 1). Anders et al. (2014) as well as Drew et al. (2013) have expanded the original AVT caldera boundary (Kellogg et al. 1994) due to recent identification of more extensive outcrops on the northern side of the plain. Outcrops of the AVT can be easily identified since the AVT is one of few biotite-bearing units in the SRP and the only one that is found within the Picabo and Twin Falls volcanic centers.

The studied stratigraphic section of the AVT consists of a glassy, well-sorted, crystal-poor (~5 %) fallout lapilli tuff, overlain by a strongly stratified lapilli tuff that grades into a massive upper welded and crystal-rich (>35 %) tuff that has a U–Pb age of 10.44 ± 0.27 Ma (Drew et al. 2013). For the purposes of this study, the lower two unwelded parts are referred to as the lower tuff (PC-12) and the upper welded part is referred to as the upper tuff (PC-14). Quartz-hosted rhyolitic melt inclusions for this study were collected from pumice clasts near the base of the stratigraphy in the fallout tuff (PC-12) and in the upper tuff (PC-14) at the type locality of the AVT, the Cove (Fig. 1).

At the Cove locality >100 m of exposed continuous section is preserved (Kellogg et al. 1994), and because no cooling breaks were observed, Drew et al. (2013) considered this sampling locality to represent a single eruption. In another location, Anders et al. (2014) reported a range in $^{40}Ar/^{39}Ar$ dates in a series of samples that they interpret as representing two $^{40}Ar/^{39}Ar$ populations corresponding to the lower and upper AVT at 10.41 and 10.22 Ma, respectively, and refer to these units as parts A and B. Anders et al. (2014) also interpret these age populations to indicate that the AVT formed as a result of two distinct eruptions, but also that the younger eruption incorporated material of the older eruption. Since the samples dated by Anders et al. (2014) are from a different location than analyzed here, we only consider these relative ages and use additional geochemical evidence to assess whether the AVT represents one eruption or two temporally or spatially separated magma bodies.

Melt inclusion and interstitial glass compositions

We studied melt inclusions and interstitial glass compositions in two representative samples of the lower (PC-12) and upper (PC-14) AVT (Fig. 2). Lower AVT melt inclusions (Fig. 3) and interstitial glass have high-silica rhyolite

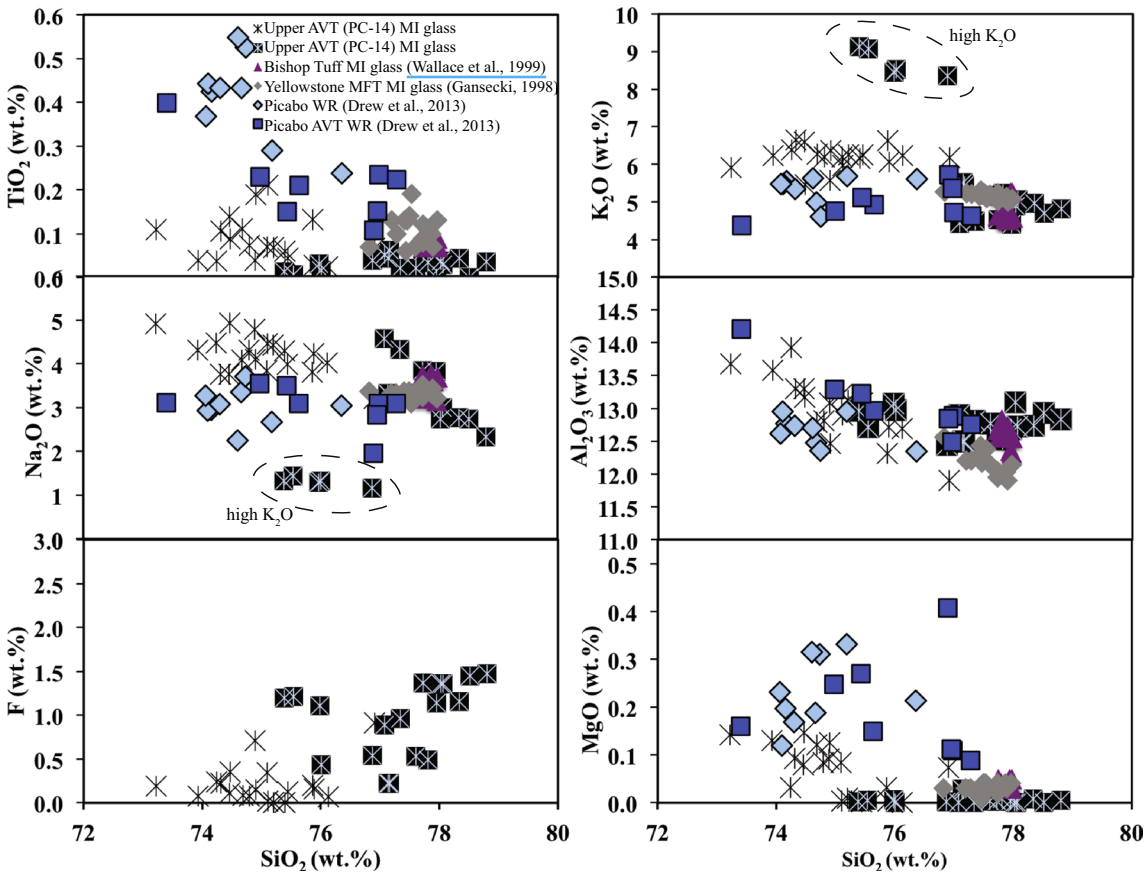

Fig. 2 Major element variations of *upper* and *lower* AVT melt inclusions and interstitial glass with SiO_2 in comparison with other Picabo whole-rock data, Bishop Tuff quartz-hosted melt inclusions, and Yellowstone MFT quartz-hosted melt inclusions

compositions (75.5–78.8 wt%; the highest SiO_2 reflects potential measurement overlap with the quartz host), very low TiO_2 (≤0.06 wt%) and MgO (≤0.03 wt%), and Al_2O_3 in the range 12.4–13.1 wt% (Fig. 2), whereas upper AVT inclusions have lower-silica rhyolite (73.2–76.9 wt%) and less differentiated compositions (Fig. 2; Table 1).

Table 1 Fourier transform infrared spectroscopic data for lower AVT quartz-hosted melt inclusions and chemical analyses for the lower and upper AVT melt inclusions

Sample	FTIR		EPMA (wt%)										
	H_2O (wt%)	CO_2 (ppm)	SiO_2	TiO_2	Al_2O_3	FeO	MgO	CaO	Na_2O	K_2O	Cl	F	Total
Melt inclusion—lower AVT (PC-12)													
PC-P1.2-1	–	–	75.54	0.007	12.71	0.77	0.005	0.45	1.43	9.08	0.07	1.21	94.67
PC-P1.2-2*	4.94 ± 0.22	196 ± 10.1	78.06	0.03	12.73	0.68	0.001	0.44	3.0	5.06	0.08	1.36	92.35
PC-P1.4*	4.69 ± 0.04	179 ± 3.1	75.98	0.03	13.07	0.72	0.007	0.46	1.29	8.44	0.08	1.11	94.55
PC-P12-2	–	–	78.52	0	12.93	0.67	0	0.45	2.74	4.7	0.08	1.45	92.43
PC-P2.2-2	–	–	77.08	0.05	12.9	0.64	0	0.33	4.57	4.43	0.07	0.89	91.82
PC-P2.6*	3.45 ± 0.07	270 ± 10.6	77.73	0.06	12.58	0.72	0.004	0.46	3.84	4.52	0.09	1.37	91.66
PC-P3.1-1*	4.59 ± 0.25	103 ± 5.7	75.38	0.01	12.96	0.73	0.002	0.46	1.32	9.13	0.08	1.2	94.29
PC-P3.1-2*	6.43 ± 0.27	145 ± 3.4	–	–	–	–	–	–	–	–	–	–	–
PC-P3.2*	5.33 ± 0.41	410 ± 33.3	78.04	0.04	13.1	0.75	0.001	0.47	2.73	4.89	0.08	1.36	92.14
PC-P3.3*	2.27 ± 0.19	120 ± 4.1	77.96	0	12.68	0.69	0.004	0.45	3.82	4.41	0.07	1.14	93.11
PC-P3.4	–	–	78.8	0.04	12.83	0.73	0.005	0.46	2.33	4.81	0.08	1.47	91.83
PC-P4.1*	3.49 ± 0.49	190 ± 48.0	77.33	0.02	12.81	0.65	0	0.37	4.33	4.48	0.06	0.96	92.57
PC-P4.2B	–	–	78.34	0.05	12.74	0.7	0.008	0.46	2.76	4.95	0.08	1.16	93.19
PC-P5.1-1*	4.79 ± 0.12	396 ± 4.4	77.16	0.06	12.5	1.06	0.03	0.47	3.28	5.44	0.12	0.22	94.68
PC-P5.1-2*	3.93 ± 0.78	393 ± 5.2	77.13	0.04	12.5	1.02	0.03	0.45	3.32	5.5	0.12	0.22	94.86
PC-P6	–	–	76.87	0.04	12.44	0.69	0.002	0.44	1.16	8.36	0.07	0.54	94.02
PC-P6.1	–	–	77.81	0.03	12.53	0.7	0.008	0.44	3.26	5.22	0.08	0.49	93.48
PC-P6.3-1*	3.84 ± 0.06	97 ± 2.7	76.01	0.02	12.97	0.7	0.001	0.45	1.32	8.53	0.08	0.43	94.3
PC-P6.3-2*	4.83 ± 0.14	79 ± 1.1	77.6	0.02	12.77	0.68	0.003	0.43	3.32	5.17	0.08	0.53	94.82
Melt inclusion—upper AVT (PC-14)													
PC-14-1	–	–	75.39	0.06	13	1	0	0	4	6	0	0	96.8
PC-14-2	–	–	75.45	0.04	13	1	0	0	4	6	0	0	97.81
PC-14-3b	–	–	74.79	0.07	12.81	1.16	0.08	0.58	4.3	6.2	0.07	0.08	97.06
PC-14-4	–	–	73.93	0.04	13.58	1.12	0.13	0.65	4.31	6.23	0.1	0.08	98.18
PC-14-5	–	–	75.88	0.03	12.72	0.83	0	0.25	4.24	6.05	0.1	0.16	97.96
PC-14-6	–	–	73.22	0.11	13.68	1.46	0.14	0.57	4.91	5.9	0.14	0.19	97.55
PC-14-7a	–	–	75.2	0.07	13.13	0.72	0.01	0.2	4.42	6.25	0.1	0	97.4
PC-14-7b	–	–	74.9	0.19	12.47	1.28	0.13	0.57	4.1	6.36	0.09	0.15	97.38
PC-14-7c	–	–	74.46	0.14	13.3	1.15	0.08	0.53	3.76	6.58	0.1	0.11	97.7
PC-14-7d	–	–	74.31	0.11	13.29	1.19	0.09	0.59	3.75	6.65	0.1	0.22	97.91
PC-14-9	–	–	76.12	0.02	12.7	0.79	0	0.11	4.02	6.23	0.09	0.07	96.91
PC-14-11	–	–	75.10	0.21	12.9	1.32	0	0.04	4.46	5.96	0.05	0.02	98.06
PC-14-12	–	–	74.24	0.04	13.92	0.64	0.03	0.26	4.48	6.39	0.07	0.24	97.35
PC-14-13	–	–	74.47	0.09	13.16	1.3	0.15	0.46	4.92	5.45	0.1	0.36	97.12
PC-14-14	–	–	74.89	0.04	13.09	1.23	0.09	0.31	4.78	5.57	0.12	0.71	97.09
PC-14-16a	–	–	74.68	0.11	12.79	1.34	0.12	0.59	4.09	6.27	0.11	0.09	96.68
PC-14-16c	–	–	76.9	0.07	11.91	0.99	0.07	0.68	3.21	6.17	0.12	0.92	98.32
PC-14-16d	–	–	75.87	0.13	12.31	0.7	0.03	0.53	3.8	6.63	0.11	0.2	96.36
PC-14-17	–	–	75.09	0.07	13.21	0.95	0.08	0.58	3.83	6.18	0.11	0.35	99.12

The asterisks indicate volatile analyses considered representative and included in subsequent figures, and underlines indicate the high K_2O inclusions. Chemical analyses are normalized to 100 % volatile free, with the exception of the total

The lower and upper AVT inclusions are peraluminous, and the major and trace element compositions of the melt inclusions show few systematic trends other than general variability.

Volatile concentrations were measured in the lower AVT melt inclusions and H_2O contents range from 2.4 to 6.4 wt%, and CO_2 contents range from 79 to 410 ppm (Table 1), corresponding to vapor saturation pressures between ~1 and 2 kbar (Fig. 4). Although the majority of melt inclusions do not contain vapor bubbles, a positive correlation between TiO_2 and CO_2 suggests vapor saturation during crystallization (Appendix Fig. 17b). Melt inclusions with lower H_2O contents but CO_2 contents equivalent to the main population of melt inclusions are likely to have experienced water loss by intracrystalline hydrogen diffusion through the quartz host (Severs et al. 2007).

In order to further assess the effect of hydrogen diffusion on the composition of the melt inclusions, we compared variations in Li and Rb to H_2O, because Li is a fast-diffusing element and Rb is a slow-diffusing element (Fig. 18; Roberge et al. 2013). A large range in Li is observed with uniform Rb concentrations, and the variability suggests that 5 of 11 inclusions likely lost some Li by diffusion. A similar pattern is observed in a plot of H_2O versus Rb (Appendix Fig. 18c), but there is no correlation

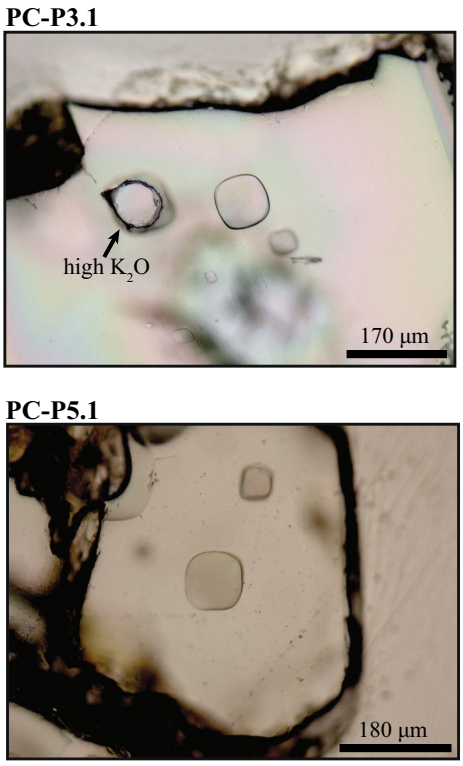

Fig. 3 Photograph of singly polished quartz-hosted melt inclusions from two samples to highlight the irregular boundary of the high K_2O inclusions

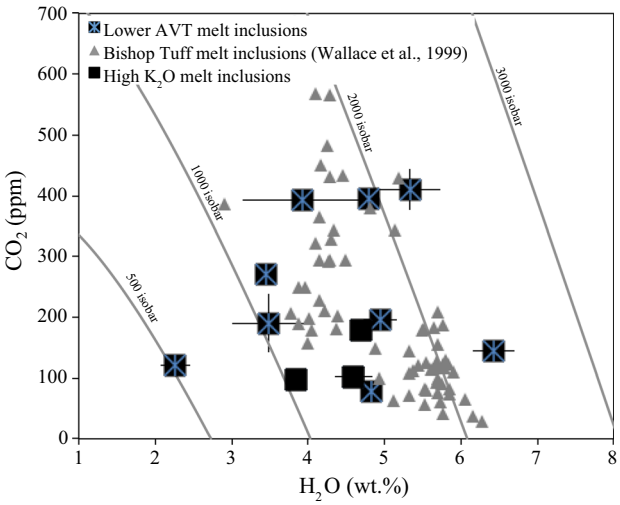

Fig. 4 Lower AVT melt inclusion CO_2 and H_2O determined by Fourier transform infrared spectroscopy in comparison with the Bishop Tuff. Isobars (at 800 °C) and the open system-degassing curve were calculated using VolatileCalc (Newman and Lowenstern 2002)

between low Li and low H_2O, making it difficult to assess how much of the variability in H_2O concentrations is due to is due to post-entrapment diffusive loss to, or exchange with, external melt. There is also no correlation between H_2O and melt inclusion size (Appendix Fig. 18d), which would be expected if variable diffusive H_2O loss occurred during final ascent. Given these relations, the main observation of the melt inclusion data is that the highly evolved and incompatible element-enriched rhyolitic melts trapped as inclusions in quartz had H_2O concentrations as high as 5–6 wt%, similar to values for other metaluminous high-silica rhyolites (e.g., Bishop Tuff; Wallace et al. 1999). More slowly diffusing elements such as Cl and most trace elements should not be affected by diffusive exchange.

Three distinct melt inclusion populations are observed in the lower AVT. These populations include the main group of melt inclusions, a group with high K_2O concentrations, and a xenocryst containing two inclusions with high Nb, Th, Ba, Ti, La, Ce, and Sm, and low Li, Pb, and B (Figs. 2, 4; Table 2). A distinctive feature of the main population of AVT rhyolitic melt inclusions is the presence of high F, up to 1.38 wt%, in comparison with Cl, which does not exceed 0.09 wt% (Fig. 5). The F greatly exceeds values typical of the Bishop Tuff (Wallace et al. 1999) and typical arc rhyolites (Wallace 2005), but the Cl is similar to values for the Bishop Tuff and lower than typical arc rhyolites (Fig. 5; Bacon et al. 1992; Wright et al. 2012). Trace element characteristics of the main population include depletions in Sr, Zr, and Ti (Table 2; Figs. 6, 7) and enrichments in Li, B, Rb, Nb, Y, Sn, Th, and U, in comparison with rhyolitic quartz-hosted melt inclusions from other silicic centers, including

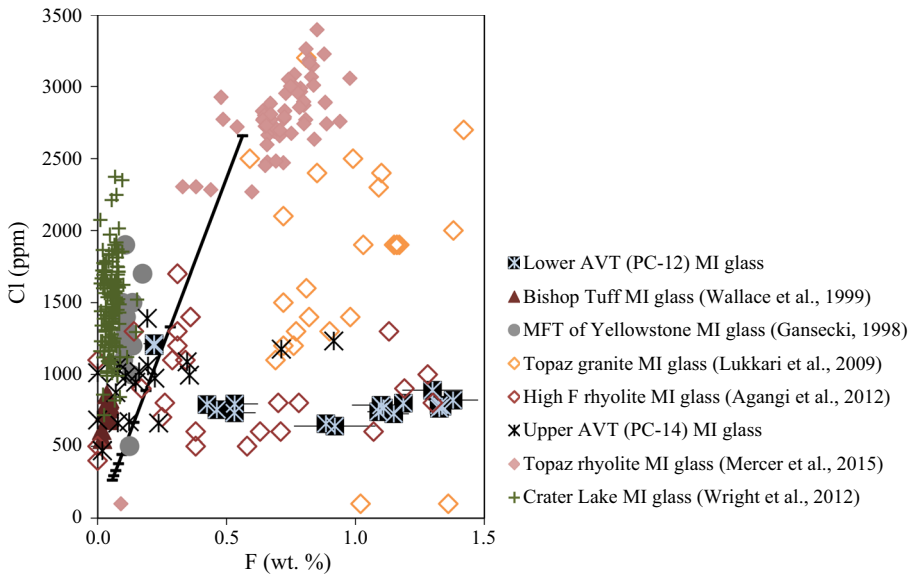

Fig. 5 F versus Cl concentration of *upper* and *lower* melt inclusions and interstitial glass in comparison with quartz-hosted melt inclusions from the Mesa Falls Tuff of Yellowstone (Gansecki 1998), Bishop Tuff quartz-hosted melt inclusions (Wallace et al. 1999), rehomogenized topaz granite inclusions (Lukkari et al. 2009), rehomogenized quartz-hosted melt inclusions from high-F rhyolites of Australia (Agangi et al. 2012), rehomogenized quartz-hosted melt inclusions from the Hideaway Park Tuff topaz rhyolite (Mercer et al. 2015), and plagioclase-hosted melt inclusions from Crater Lake (Wright et al. 2012). The *solid line* represents a fractional crystallization curve from a Yellowstone basalt (Stefano et al. 2011) with starting compositions of Cl and F of 266 ppm and 0.06 wt%, accordingly with tick marks at increments of 10 %

the Mesa Falls Tuff (MFT) of Yellowstone and the Bishop Tuff (Wallace et al. 1999; Gansecki 1998; Fig. 8).

In comparison with this main population of melt inclusions, there are five high K_2O inclusions (8.4–9.1 wt%; Figs. 2, 3) and two inclusions within a xenocryst, which have distinct trace element compositions (Figs. 2, 8) and are hosted in the same quartz phenocryst. The higher K_2O (8.4–9.1 wt%) inclusions have lower Na_2O and SiO_2, although they are within the range of H_2O and CO_2 concentrations of the main population of AVT melt inclusions and indistinguishable in trace element characteristics from the main population. The xenocryst-hosted inclusions have high MgO and FeO, low F, and very different trace element concentrations. The difference between these two inclusions and the average composition of the AVT melt inclusions include, but is not limited to, higher LREEs, Ti, Ba, and Th concentrations, and lower B and Rb concentrations (Figs. 6, 7, 8).

The upper AVT melt inclusions are lower in SiO_2 and generally contain higher K_2O, Na_2O, MgO, and Al_2O_3 concentrations than lower AVT melt inclusions (Fig. 2). However, the upper AVT inclusions as a group have a larger range in major element concentrations than the main population of lower AVT inclusions (Fig. 2). The upper AVT also has significantly lower F concentrations, reaching a maximum of 0.92 wt% F (average 0.23 wt% F). Cl concentrations range from 0.05 to 0.14 wt%. These Cl concentrations are similar to values for the Bishop Tuff (Wallace et al. 1999); however, the F concentrations exceed the Bishop Tuff and typical arc rhyolites (Wallace et al. 1999; Wallace 2005; Fig. 5).

The main population of AVT melt inclusions shows 2–3× the concentration of incompatible elements in the least evolved AVT whole-rock composition, but the interstitial glass composition falls within the range of the melt inclusion glass for U, Th, Rb, and Nb. The differences between the lower AVT whole-rock and melt compositions can largely be attributed to the crystal content. The crystallization of accessory phases, allanite, chevkinite, and apatite, is also required to match the concentrations in detail. There are large trace element differences in the interstitial glass of the upper and lower AVT (Fig. 8) that roughly correspond to the whole-rock trace element differences. The trace element interstitial glass composition of PC-12 overlaps with the PC-12 melt inclusions compositions.

The AVT melt inclusion major and trace element compositions indicate extreme differentiation, with Sr/Rb and Ba/Rb ratios of <0.002 and 0.009, respectively (Fig. 8c). Trace element concentrations indicate crystallization of the mineral assemblage of quartz, plagioclase, sanidine, and biotite as well as accessory minerals: zircon (low Zr), allanite, and chevkinite (low LREEs). Relative to other Picabo rhyolites, the AVT melt inclusions show enrichment in U relative to Th and enrichment in Rb relative to

Table 2 Trace element chemical analyses for the lower AVT melt inclusions

	LA-ICP-MS (ppm)												
	Li	B	P	Ca	Ti	Rb	Sr	Y	Zr	Nb	Ba	La	Ce
Melt inclusions lower AVT (PC-12)													
PC-P1.2-1	17.4	89.7	59	2833	178	564	0.16	138	81.0	61.0	0.23	8.14	26.2
PC-P1.2-2*	130	97.6	60	2958	136	574	bdl	151	87.3	52.4	0.09	7.25	21.8
PC-P1.3	139	99.6	66	2407	133	561	bdl	144	84.1	53.5	0.03	6.67	22.7
PC-P1.4*	0.6	90.4	42	2325	143	604	0.03	133	75.3	54.6	0.14	6.70	21.4
PC-P2.2-2	132	87.1	59	2395	135	528	0.06	145	90.7	63.7	0.09	6.77	22.2
PC-P2.6*	144	95.1	54	3022	148	551	bdl	144	84.5	57.1	0.24	7.04	22.6
PC-P3.1-1*	4.1	79.1	6	2802	138	522	0.12	135	81.3	57.2	0.07	6.67	21.3
PC-P3.1-2*	138	96.1	57	3012	143	548	0.03	142	85.7	54.3	0.15	7.68	23.1
PC-P3.3*	151	102	46	3081	144	578	0.17	153	94.8	60.3	0.07	8.38	25.6
PC-P4.2B	97.6	89.6	50	2969	124	547	0.10	130	77.6	51.9	0.11	6.62	21.9
PC-P5.1-1*	39.3	32.4	69	3165	377	287	0.56	98	99.9	112	2.68	21.3	59.7
PC-P5.1-2*	41.4	39.4	66	2696	321	276	0.39	102	82.7	113	1.21	15.6	45.3
PC-P6.3-1*	51.9	90.5	102	2699	127	514	0.11	129	79.6	48.9	0.12	6.14	19.6
Matrix glass (trace elements only)													
PC-12 (lower AVT)			46		138	529	1.0	137.3	92.1	53.7	2.4	7.9	24.2
PC-14 (upper AVT)			236		165	163	38.3	51.9	18.6	9.8	718	115	168
PC-76			78		377	278	15.6	10.9	30.9	14.8	233	32.6	53.2

	LA-ICP-MS (ppm)												
	Pr	Nd	Sm	Eu	Gd	Dy	Er	Yb	Hf	Ta	Pb	Th	U
Melt inclusions lower AVT (PC-12)													
PC-P1.2-1	3.50	16.7	8.24	bdl	12.5	19.2	13.4	16.3	6.55	10.5	78.0	30.9	18.7
PC-P1.2-2*	3.11	14.9	8.24	bdl	13.1	19.9	14.1	17.0	7.48	10.3	70.5	30.2	17.4
PC-P1.3	3.21	14.4	8.98	bdl	11.7	17.2	13.6	14.1	7.14	9.63	78.5	28.5	18.6
PC-P1.4*	2.85	14.9	7.53	bdl	12.3	17.7	13.5	15.1	5.25	10.9	77.9	27.8	17.2
PC-P2.2-2	3.50	14.7	7.61	bdl	11.5	18.4	14.2	15.8	6.44	11.4	68.3	29.6	20.1
PC-P2.6*	3.39	15.5	8.31	bdl	12.0	19.3	14.1	17.2	6.86	11.2	72.4	31.0	18.0
PC-P3.1-1*	3.12	15.2	6.97	bdl	11.0	16.4	14.0	13.5	5.82	9.61	68.3	26.9	16.4
PC-P3.1-2*	3.13	15.2	8.06	bdl	13.0	19.1	12.8	16.3	6.83	9.98	78.4	31.4	18.7
PC-P3.3*	3.74	16.6	8.21	bdl	12.3	19.1	14.4	16.9	7.38	11.0	78.3	32.7	19.2
PC-P4.2B	3.07	13.3	7.29	bdl	11.3	15.5	12.0	14.8	5.73	8.91	74.3	27.9	18.0
PC-P5.1-1*	7.08	31.6	11.0	0.05	14.6	20.0	12.5	10.5	4.93	4.52	58.8	40.3	15.4
PC-P5.1-2*	5.45	24.9	10.9	bdl	12.4	20.0	12.5	11.5	3.90	4.87	55.5	41.1	16.4
PC-P6.3-1*	2.84	15.0	7.06	bdl	10.7	16.7	12.4	16.6	5.81	9.76	73.2	27.4	17.5
Matrix glass (trace elements only)													
PC-12 (lower AVT)	3.2	16.7	8.2	0.004	11.2	17.0	12.4	15.6	6.9	9.9	67.5	31.0	16.0
PC-14 (upper AVT)	22.0	89	14.1	1.4	13.5	10.7	4.8	4.0	1.4	2.5	42.4	20.4	4.8
PC-76	4.9	17.6	2.8	0.4	1.9	2.0	1.2	0.9	1.9	2.2	32.7	12.5	2.8

SiO_2 content of each inclusion was used as the internal standard. The abbreviation bdl represents analyses that were below detection limits. The average percent error reported is the average percent difference between measured concentrations of the standard and the actual value. With the exception of Nb, which has a percent error of 10.39 % P, all other reported elements have an error less than 10 %

Nb (Fig. 8a, b). The main population shows equal incompatibility of Nb and Rb, and greater incompatibility of U than Th, in contrast to the less differentiated inclusions, which demonstrate greater incompatibility of Nb than Rb, and equal incompatibility of U and Th. The two inclusions within the xenocryst have contrasting trace element concentrations including higher Cl, Th, Nb, Sr/Rb and Ba/Rb (Figs. 5, 8).

The five inclusions with high K_2O all have irregular boundaries (Fig. 3). The characteristics of these inclusions

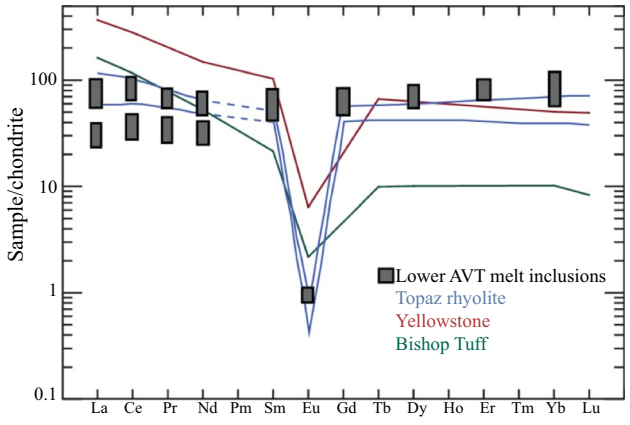

Fig. 6 Rare earth element diagram of lower AVT melt inclusions, Wah Wah Mountains topaz rhyolites (Christiansen et al. 2007), Mount Bennett Hill rhyolite of the SRP (Honjo 1990) and Bishop Tuff rhyolite (Hildreth 1977; modified from Glazner et al. 2008). All trace elements are normalized to chondrite values (Sun and McDonough 1989). *Gray bars* correspond to the range spanned by the AVT melt inclusion data, on the left side where there is separation represents the compositional distinction between the two most primitive inclusions and the main population of melt inclusions

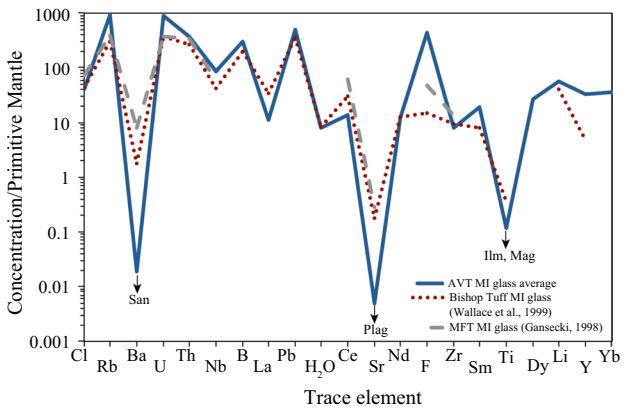

Fig. 7 Spider plot of lower AVT melt inclusions in comparison with Bishop Tuff and Mesa Falls Tuff (MFT) melt inclusions. Trace elements are normalized to the primitive mantle (McDonough and Sun 1995)

cannot be analytical artifacts or produced by igneous crystallization. A possible interpretation is that these inclusions were originally reentrants (unsealed inclusions) that were subsequently altered to sericite, reincorporated into rhyolitic magma, and then had additional overgrowths of quartz (discussed below).

CL zoning patterns and Ti in host quartz

The CL images of the host quartz grains provide petrologic insight into the crystal growth histories and the changes in crystallization conditions, which are texturally tied to the analyzed composition of the melt inclusions (Fig. 9). Distinct CL features of quartz grains with melt inclusions include both bright CL rims and cores (bright cores: 12.5 % of grains, bright rims: 19 % of grains), and prevalent truncated zones of oscillatory zoning (Fig. 9). Comparison of the CL images with whole-quartz phenocrysts from the lower fallout and upper ignimbrite (refer to phenocrysts on Fig. 9 and in Appendix B) revealed that only phenocrysts from the lower airfall tuff had bright cores (Appendix Fig. 15). Although the bright cores in the lower tuff do not have large increases in Ti concentrations compared to the rims, the boundaries between zones are extremely sharp. Larger Ti variations and thicker CL zones (up to 250 μm) are present in the quartz grains from the upper tuff, with less evidence for small-scale oscillatory zoning. The majority of Ti measurements of melt inclusion host quartz grains (of the lower fallout) were less than 60 ppm, with the occasional bright rims and cores reaching concentrations greater than 60 ppm, but not exceeding 82 ppm. One exception is an outermost bright rim that had a Ti concentration of 276 ppm. Quartz CL patterns and Ti measurements of the upper crystal-rich portion of the deposit yielded significantly higher Ti concentrations and a wider range of variation from <60 to 196 ppm Ti (Appendix C). The Ti concentration of the lower AVT quartz overlaps the upper AVT concentrations, but is on average significantly lower.

$\Delta^{18}O_{Qz\text{-}Mt}$ temperatures

Magnetite and quartz were extracted from single, rapidly quenched pumice clasts in the lower (PC-12) and upper (PC-14) tuff, and the $\delta^{18}O$ values measured were used in conjunction with additional quartz $\delta^{18}O$ from Drew et al. (2013) from the same samples to estimate magma temperature and melt $\delta^{18}O$. The $\delta^{18}O_{Mt}$ of the upper tuff ranges from 3.87 to 3.79 ‰, the freshest magnetite from the lower tuff is 2.44 ‰, and the $\delta^{18}O$ values of quartz in the upper and lower tuff are 8.41 and 8.83 ‰, respectively. The $\Delta^{18}O_{Qz\text{-}Mt}$ temperatures (using 6.29 A-factor from Chiba et al. 1989) is 892–906 °C for the upper tuff, and 719 °C for the lower tuff, indicating a large (~180 °C) temperature difference between the upper and lower tuffs, twice the difference between the lower and upper Bishop Tuff (e.g., Hildreth and Wilson 2007; Bindeman and Valley 2002). Using these temperatures and $\delta^{18}O_{Qz}$, we estimated the $\Delta^{18}O_{Qz\text{-}Melt}$ fractionations to be 0.47 and 0.37 ‰, respectively (Bindeman and Valley 2002). The computed $\delta^{18}O_{melt}$ values for these different temperatures are 8.4 ‰ (PC-12, lower tuff) and 8.0 ‰ (PC-14, upper tuff), suggesting a subtle but recognizable ~0.4 ‰, isotopic difference between the upper and lower tuff. This isotopic difference is coupled with Sr isotopic differences between whole-rock samples of the lower and upper tuff (0.73443 and 0.71507, respectively; Drew et al. 2013).

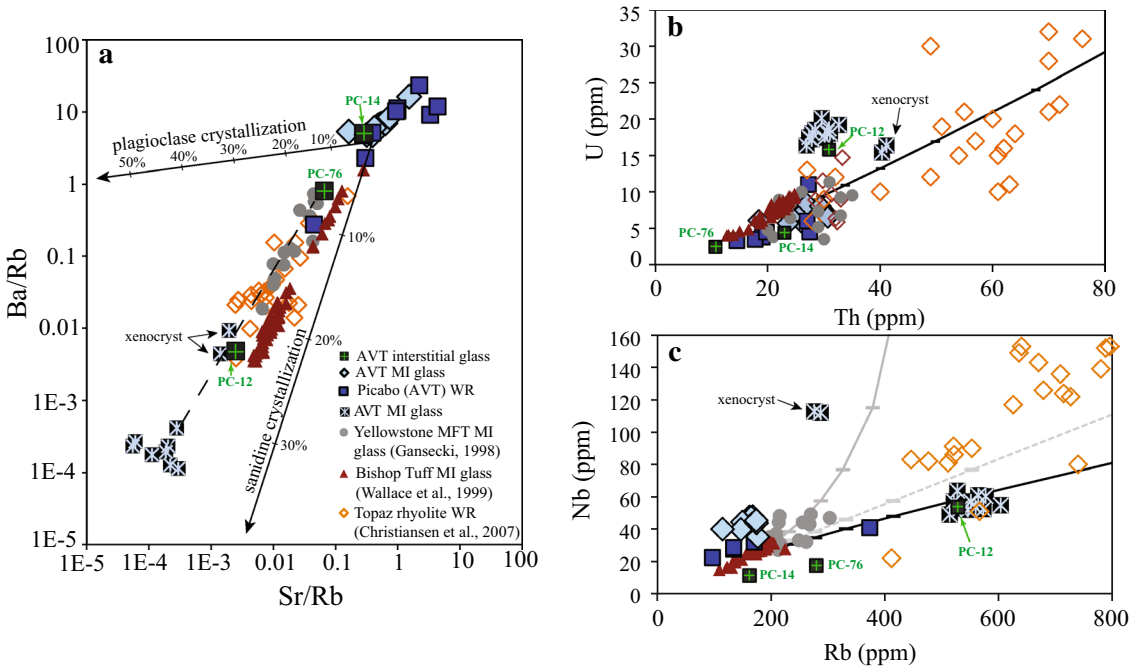

Fig. 8 Trace element compositions of lower AVT melt inclusions and interstitial glass in comparison with Picabo rhyolites, topaz rhyolites and granite, Bishop Tuff melt inclusions, and Mesa Falls Tuff melt inclusions. **a** Sr/Rb variations with Ba/Rb of AVT melt inclusions and interstitial glass. The *solid lines* represent fractional crystallization trends of plagioclase and potassium feldspar (Anderson et al. 2000). The *dashed line* emphasizes the correlation between the AVT melt inclusions and MFT melt inclusions. **b** U versus Th of AVT melt inclusions and interstitial glass. The *black line* represents fractional crystallization at 10 % increments beginning at a low silica rhyolite composition. This fractional crystallization line assumes a mineralogy representative of typical Yellowstone hotspot rhyolites (Watts et al. 2011) and bulk partition coefficients of 0.137 and 0.154, and initial concentrations 6 and 10 ppm for U and Th, accordingly. **c** Nb versus Rb of AVT melt inclusions and interstitial glass. The *gray and dotted gray curves* represent equilibrium crystallization at 10 % increments beginning at a low silica rhyolite composition (Rb: 166 ppm, Nb: 23 ppm). The partition coefficients were $D_{Nb} = 0$, 0 and $D_{Rb} = 0$, 0.298 for the *dotted gray* and *gray curves* accordingly. The *black curve* represents fractional crystallization at 10 % increments beginning at a low silica rhyolite composition (Rb: 166 ppm, Nb: 23 ppm). The partition coefficients were $D_{Rb} = 0$ and $D_{Nb} = 0.2$. The black fractional crystallization curve assumes partition coefficients of 0.7 and 0.2 and initial concentrations of 166 and 23 for Rb and Nb, respectively. The gray fractional crystallization curve assumes partition coefficients of 0

Discussion

What do the quartz phenocrysts and melt inclusions represent in the magmatic system?

The composition of melt inclusions from the upper and lower tuff, the position of melt inclusions with respect to CL zoning in quartz (Fig. 9), and the interstitial glass compositions provide insight into the evolution of magmas that erupted to form the AVT. The fallout of the lower AVT (PC-12) is the first eruptive product from the Picabo volcanic center, and therefore, it provides information about magmatic processes leading to volcanism initiation. The upper AVT (PC-14) is the subsequent eruptive product that is more chemically and isotopically similar to typical "hot and dry" SRP rhyolitic compositions, indicating a potential connection between extreme "off-SRP plume axis" or Basin and Range type rhyolites (Christiansen 2005; Christiansen et al. 2007) and more typical rhyolites of the SRP and subsequent volcanism at the Picabo eruptive center (Drew et al. 2013).

The different populations of lower AVT melt inclusions and textural constraints of complex CL textures in both the lower and upper tuffs suggest that quartz phenocrysts underwent a protracted history of growth and resorption. Although the melt inclusions are highly differentiated in composition (Figs. 2, 8), the trace element similarity (especially Nb, Rb, U) between the interstitial glass and many of the melt inclusions in the lower AVT, and their linear co-variations on binary diagrams (Fig. 8), demonstrates that the majority of quartz phenocrysts and their melt inclusions are not random xenocrysts but contain information about the formation processes of the AVT magma. Only one phenocryst containing two melt inclusions with contrasting trace element characteristics to the main melt inclusion population is interpreted to be a xenocryst.

High-K_2O melt inclusions in the lower AVT (Figs. 2, 9) require additional discussion because peraluminous igneous crystallization is not capable of producing 7–9 wt% K_2O

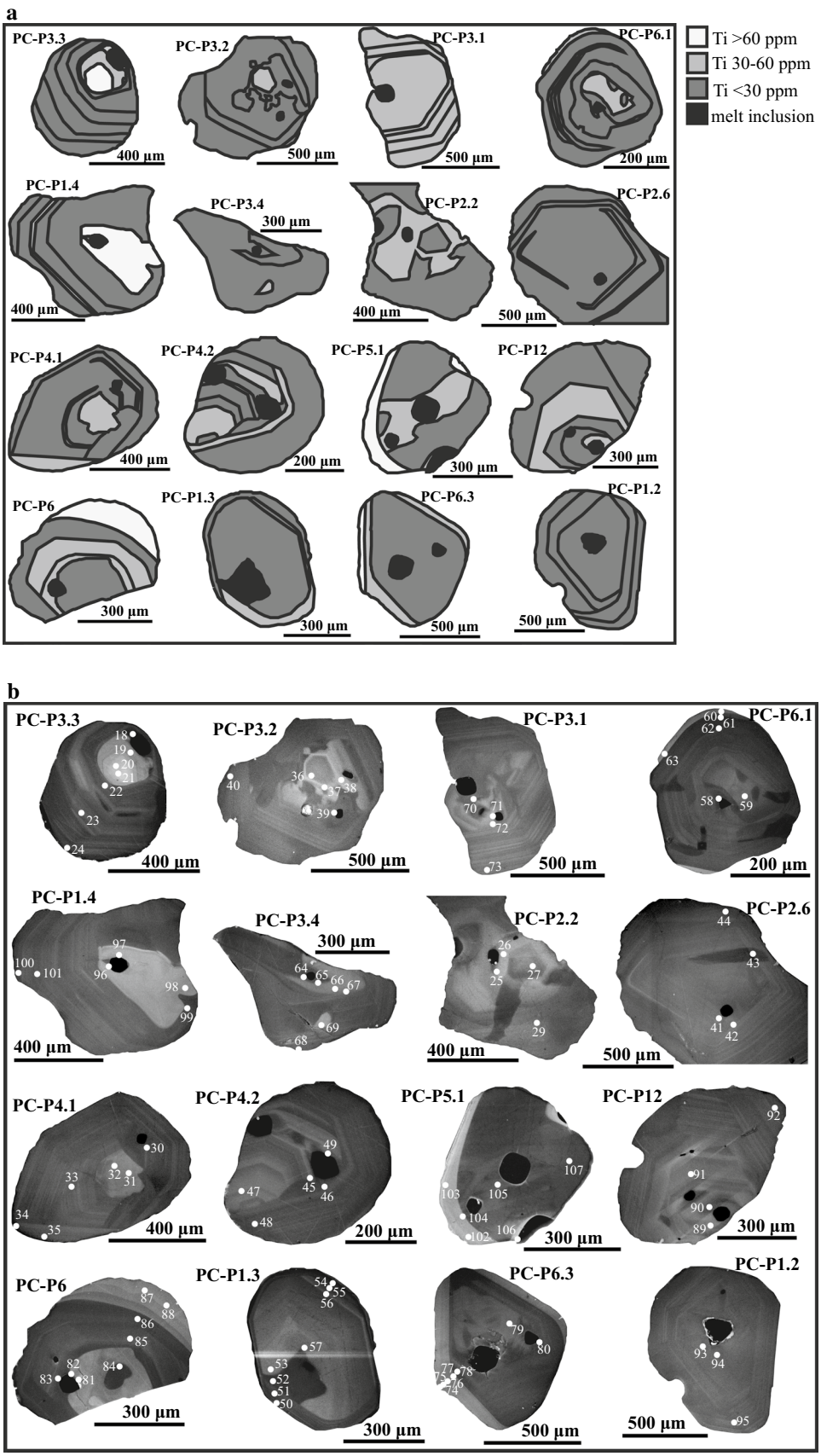

Fig. 9 **a** Annotated cathodoluminescence maps, highlighting zoning patterns and Ti concentrations in melt inclusion host quartz phenocrysts of the lower AVT. The zones shown are extrapolated based on the Ti differences measured at the points shown and distinct CL boundaries. Melt inclusions are shown in *black* and Ti concentrations are shown by three different colors representing less than 30 ppm Ti (below instrument detection limits), between 30 and 60 ppm Ti, and greater then 60 ppm Ti. **b** Cathodoluminescence images of melt inclusion host quartz phenocrysts of the lower AVT. Numbered points are where Ti and Al concentrations were measured

and reduced Na_2O (Peccerillo and Taylor 1976). The host quartz of the high-K_2O inclusions encompasses the range of CL zoning observed (Fig. 7) and one inclusion, PC-P6.3, even contains one high K_2O inclusion and one normal K_2O melt inclusion in the same CL zone. Glass weathering upon secondary hydration (Jezek and Noble 1978) or formation of hydrothermal sericite with loss of Na_2O and gain of K_2O during mica formation could produce these signatures. Therefore, these melt inclusions may represent reentrants altered to sericite (muscovite-bearing) that were remelted and/or resealed. We discount the possibility of extreme K_2O gain through quartz or a crack, because no such high K_2O composition exists in the groundmass. We prefer the sericite alteration interpretation to that of Szymanowski et al. (2015) who interpreted up to 11 wt% K_2O in melt inclusions with 60 wt% SiO_2 to be a result of "hidden" igneous differentiation of an intermediate magma.

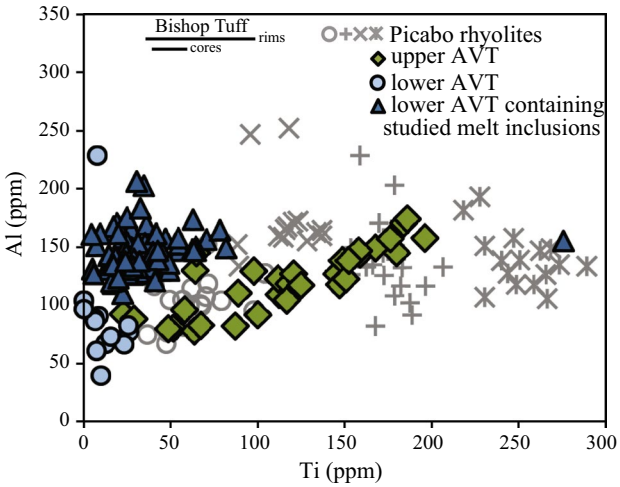

Fig. 10 Ti and Al trace element variations in quartz from the upper and lower AVT in comparison with quartz of the Bishop Tuff. Quartz from the entire Bishop Tuff eruptive sequence spans 44.3–57.2 ppm in the cores and 39.8–98.2 ppm in the rims (Wark et al. 2007)

Ti-in-quartz variations across the eruptive stratigraphy and implications for magmatic temperatures

CL imaging and Ti concentrations of quartz reveal great complexity in phenocrysts from the upper and lower tuff (Fig. 9). Each quartz grain demonstrates different patterns of fragmentation, dissolution, and overgrowth during multi-stage heating and cooling episodes. The CL zoning patterns (e.g., truncated oscillatory zones, bright cores, bright rims, and changing Ti concentrations) of quartz in relation to the location of the melt inclusion also suggests at least one and as many as four resorption events since entrapment of the inclusion. For example, PC-P1.2 displays the simplest CL zoning with likely only one resorption and regrowth event, whereas PC-P6, PC-P4.1, PC-P4.2, and PC-P1.3 display the most complex zoning with approximately four episodes of dissolution or fragmentation and regrowth (Fig. 9). The melt inclusion position enclosed in the specific CL zones (Fig. 9) suggests that they were able to survive one or more reheating episodes, thus recording earlier stages (pre-fragmentation, dissolution of crystal growth) of magma generation.

The lower Ti concentrations (average 32 ppm) of quartz in the lower AVT (PC-12) compared with the higher concentrations (average 116 ppm) in the upper AVT (PC-14; Fig. 10) are consistent with higher temperatures, higher pressures, and/or lower TiO_2 activity in the upper AVT (e.g., Huang and Audetat 2012; Wark and Watson 2006; Thomas et al. 2010, 2015). These Ti differences are broadly in agreement with the 180 °C higher $\Delta^{18}O_{Qz\text{-}Mt}$ isotopic temperature estimate for the upper AVT. Calculation of absolute temperatures from Ti-in-quartz requires assumptions about melt TiO_2 activity, pressure, and growth rate (Wilson et al. 2012; Huang and Audetat 2012). In order to calculate approximate temperatures based on the Ti concentration, we assume a pressure of 2 kbars based on the maximum entrapment pressure of the lower AVT melt inclusions. Using the average Ti concentration of 32 ppm in quartz from the lower tuff and a TiO_2 activity of 0.6, the Huang and Audetat (2012) Ti-in-quartz calibration yields a temperature of 654 °C. In comparison, a TiO_2 activity of 0.35 used for topaz rhyolite melt inclusions (Mercer et al. 2015) yields a temperature of 793 °C. The presence of allanite in the lower tuff (McCurry 2009), however, constrains temperatures to <765 °C (Vazquez et al. 2004), thus bracketing the temperature between ~654 and 765 °C for the lower tuff, in broad agreement with the ~719 °C estimate using $\Delta^{18}O_{Qz\text{-}Mt}$.

The upper tuff has higher and more variable quartz Ti concentrations (<30–196 ppm), and within one phenocryst reaches a maximum Ti range of 82 ppm. The large range in Ti of the upper AVT suggests that quartz grains could have been recycled from melts with different Ti concentrations. If we assume that the upper and lower tuffs crystallized at a constant pressure and TiO_2 activity, then the temperature range for the average Ti content of 116 ppm would be 809–890 °C (a_{TiO2} of 0.6 and 0.35, accordingly). At lower pressures (1.5 kbar), the temperature range would be reduced to 785–865 °C. At the maximum Ti observed in the upper AVT (196 ppm), the potential temperature range (at 2 kbar) would be 888–981 °C (a_{TiO2} of 0.6 and 0.35, accordingly).

Based on average Ti concentrations in quartz, the upper AVT would be approximately 100 °C hotter than the lower AVT and individual quartz crystals within the upper AVT record a larger temperature range. The range in temperature and abrupt CL changes emphasizes that the quartz from the upper tuff experienced significant changes in magmatic

conditions. Repeated reheating and mixing within the upper AVT magma body could have contributed to the CL zoning observed (terminations and overgrowths). A temperature increase greater than 50 °C could have provided the necessary overpressure inside melt inclusions to cause fracturing (Bindeman 2005), and these grains could have later become overgrown.

These estimated temperatures also demonstrate that the temperature of the lower AVT is significantly less than that of other rhyolites of the Picabo volcanic center, which have an average pre-eruption temperature of 850 °C (Drew et al. 2013) similar to other hot and dry rhyolites of the Snake River Plain (Cathey and Nash 2004). The large ~100 °C temperature difference between the lower and upper tuffs is greater than that observed within the Bishop Tuff (ca 100 °C or 710–810; Hildreth 1979; Bindeman and Valley 2002; Wark et al. 2007), and likely cannot have existed in the same magma system without convection, vertical mixing, or conductive decay. This temperature range further supports the interpretation that the upper and lower AVT originated from two temporally and/or spatially separated magma bodies or eruptions.

Evidence for two separate magma bodies and their state at the time of the eruption

Several lines of evidence reinforce the conclusion that the upper and lower AVT represent two temporally and/or spatially separated magma bodies.

This evidence includes:

1. Distinct differences in the trace element and major element concentrations of the interstitial glass and melt inclusions of the upper and lower AVT (Fig. 2).
2. Distinct Sr and Nd isotopic values between units (0.72520–0.71488; Drew et al. 2013).
3. Subtly distinct $\delta^{18}O_{melt}$ values (7.9–8.3 ‰).
4. Large differences in temperature, which are impossible to sustain in a single magma chamber ($\Delta^{18}O_{qtz\text{-}mg}$ and Ti in quartz).

The major element whole-rock and interstitial glass chemistry, oxygen and strontium isotopes, and Ti concentrations in quartz of the upper and lower AVT represent major differences between the two erupted tuffs. In addition, many of the melt inclusions in the upper AVT are lower-silica rhyolites and contain less fractionated major element compositions and lower F concentrations than the lower AVT, with only a few inclusions that trend toward the F concentrations of the lower AVT. The interstitial glass of the upper AVT largely falls in the range of the trace element composition of other SRP rhyolites (Fig. 8). In contrast, the magma of the lower AVT represents a highly fractionated "off axis" wet and lower-temperature rhyolite composition, whereas low-F portions of the upper AVT are more similar to SRP-type, hot and dry rhyolite. However, all units in the AVT are more hydrous than typical SRP rhyolites, as demonstrated by the occurrence of biotite.

The isotopic and chemical characteristics of the lower AVT demonstrate that the magma bodies evolved separately. Samples of the AVT collected elsewhere in this region of the SRP are also consistent with two separate eruptions, specifically Ar–Ar dating interpretations by Anders et al. (2014) (lower AVT: 10.41 Ma and upper AVT 10.22 Ma). After eruption of the lower AVT, it is possible that the upper AVT magma mingled with the lower AVT residuum at depth. Since the upper AVT is higher temperature, quartz recycled from the lower AVT (with lower Ti quartz) would undergo resorption leaving little direct evidence for magma mingling, other than the CL textural evidence of resorbed quartz. However, a more extensive dataset for upper AVT melt inclusions would be needed to investigate this association.

Comparison with other rhyolites from different tectonic settings

To highlight the distinct chemical features of the AVT melt inclusions, we have compared their compositions, including F and Cl concentrations, to that of the following contrasting silicic systems: (1) stratified magma bodies: Bishop Tuff quartz-hosted rhyolitic melt inclusions (Wallace et al. 1999; Roberge et al. 2013; Anderson et al. 2000) and subduction-related Crater Lake plagioclase-hosted melt inclusions (Bacon et al. 1992; Wright et al. 2012); and (2) "intraplate, A-type" rhyolites: Mesa Falls Tuff of Yellowstone (Gansecki 1998), Almeev et al. (2012) experimental determinations of the Bruneau Jarbidge rhyolites, rehomogenized (Agangi et al. 2012) and rehomogenized topaz rhyolite melt inclusions (Mercer et al. 2015), and topaz rhyolite whole-rock data (Christiansen et al. 2007). We only discuss slow-diffusing elements from the rehomogenized inclusions (F, Cl, Rb, Nb, Ce) due to the possible effects of hydrogen diffusion during initial cooling and the rehomogenization process.

The Bishop Tuff is a classic, well-studied example of a stratified magma chamber (Hildreth 1979; Wallace et al. 1999; Anderson et al. 2000; Roberge et al. 2013; Hildreth and Wilson 2007; Chamberlain et al. 2015), and therefore serves as a means to compare the chemical signatures of zoned magma chambers, although there are contrasting views by Gualda and Ghiorso (2013). The H_2O contents (2.4–6.4 wt%) of the glassy lower AVT quartz-hosted rhyolitic melt inclusions extend to high values that are similar to the Bishop Tuff melt inclusions (Fig. 3; Wallace et al. 1999; Roberge et al. 2013), but are higher than what is

expected for the hot and dry, densely welded rhyolites considered typical of the SRP (1–3 wt%; Almeev et al. 2012). The similarity of these water contents is reinforced by the (lower) temperature agreement between the lower AVT and Bishop Tuff (estimated from Ti-in-quartz and $\Delta^{18}O_{qz\text{-}mt}$). Although the lower AVT melt inclusions have similar overlapping major element compositions with the Mesa Falls Tuff and Bishop Tuff, they have contrasting trace element trends especially for REEs and LILEs (Figs. 6, 7). Most notably, the lower AVT melt inclusions have F concentrations that are an order of magnitude greater than that of both the Bishop Tuff and Crater Lake volcanics, and comparable to that of other high-F topaz rhyolites found worldwide (Christiansen et al. 1984, 2007; Burt et al. 1982; Mercer et al. 2015). The major element composition of the upper AVT differs from the Bishop Tuff and Mesa Falls Tuff, specifically in Na_2O, MgO, Al_2O_3, and K_2O. The upper AVT also has more heterogeneous major element compositions than the lower AVT, the Bishop Tuff and the Mesa Falls Tuff. However, the Cl and F concentrations of the upper AVT, although heterogeneous, overlap with the Bishop Tuff and Mesa Falls Tuff, but extend toward more enriched lower AVT melt inclusion populations.

The high F in the rhyolitic melt inclusions of the AVT suggests an inherent similarity to topaz rhyolites. Topaz rhyolites contain quartz, sanidine, Na-plagioclase, and accessory fluorite and occasionally topaz (Christiansen et al. 2007). The AVT has a similar mineralogy, and Trimble and Carr (1976) reported topaz, which likely formed by vapor phase crystallization, in the lower AVT in regions near the American Falls reservoir. Characteristics typical of topaz rhyolites include high F concentrations in glass (0.2–2 wt%), enriched lithophile elements, flat REE patterns with negative Eu anomalies, F/Cl ratios >3, high Fe/Mg, low fO_2 (near the QFM buffer), A-type granite chemical compositions, and low, near-solidus crystallization temperatures of ~650–700 °C (Christiansen et al. 2007).[1] The trace element concentrations of the lower AVT melt inclusions demonstrate overlapping characteristics with topaz rhyolites (Figs. 5, 6, 7, 8). More specifically, comparison of the geochemistry of the lower AVT melt inclusions and topaz rhyolites demonstrates that the lower AVT melt inclusion glass trends toward the more evolved Wah Wah topaz rhyolite compositions (Christiansen et al. 2007). The lower AVT whole-rock data and interstitial glass also overlap the topaz rhyolites for many trace elements (Fig. 8), with the exception of elements such as Nb and Rb that would be affected by the presence of late-stage accessory phases.

[1] Topaz rhyolites have been associated with the northern segments of the Rio Grande Rift (Wegert et al. 2013), opening of the Nevada rift (Stewart et al. 1975; Zoback and Thompson 1978; John et al. 2000), extension in the Great Basin (Zoback et al. 1981), detachment faulting in western Arizona (Suneson and Lucchitta 1983), and back-arc graben formation (Armstrong 1978). Christiansen et al. (2007) stresses the spatial and temporal association of topaz rhyolites with both extension and previous subduction-related calc-alkaline magmatism.

Mass balance of the volatile budget with isotopic and chemical constraints

The whole-rock $^{87}Sr/^{86}Sr$ and $^{143}Nd/^{144}Nd$ isotopic data of Drew et al. (2013) coupled with melt inclusion H_2O, CO_2, F, Cl, and trace element constraints from this study have enabled us to assess the mantle and crustal sources and the processes that contribute to rhyolite generation. We first investigate the feasibility of generating rhyolites with incompatible element enrichments, especially F, through traditional mechanisms of crustal melting and fractional crystallization. Whole-rock, interstitial glass, and melt inclusion glass compositions provide insight into the evolving melt chemistry. A previous Sr and Nd isotopic mass balance for the AVT by Drew et al. (2013) demonstrated that ~50 %, by mass, of the AVT is derived from upper Archean crust, providing isotopic constraints on the geochemical evolution. Below we consider potential sources for H_2O, F, and Cl using trace element crustal compositions (Rudnick and Gao 2003) and basalt compositions (McDonough and Sun 1995; Michael and Cornell 1998). There is a great deal of diversity of volatile contents in the crust and basalts depending on the lithology and source of melting; however, we use these compositions as a first-order approximation for fractional crystallization and crustal batch melting calculations.

Sources for water

Our AVT melt inclusion data include the highest H_2O values (up to 6.5 wt%) reported for the SRP so far. The Sr–Nd isotopic constraints by Drew et al. (2013) show that 50 % of the AVT was derived from crustal melting. Dehydration melting of Archean granulite or amphibolite requires a high melt fraction for melt segregation (e.g., Wickham 1987); however, at the required high melt fractions, crustal melts only contain ~1 wt% H_2O (Patiño Douce and Beard 1995; Thompson 1982; Clemens 1990). Therefore, it seems likely that much of the H_2O in the lower AVT magma ultimately came from differentiates of mantle-derived basaltic magma, which would also provide the necessary heat for crustal melting. Partial melting (5 %) of enriched mantle can produce basaltic melts with 1 wt% H_2O, and extensive fractional crystallization of these could produce derivative melts with 4 wt% water after 75 % crystallization. At a basaltic differentiate and crustal melt ratio of approximately 1:1, as is indicated by $^{87}Sr/^{86}Sr$ and $^{143}Nd/^{144}Nd$ (Drew et al. 2013), the resulting hybrid magma would contain ~3 wt% H_2O, with basaltic differentiate contributing 2.5 wt% of this total and

crustal anatexis contributing 0.5 wt%. Therefore, more fractional crystallization is required to reach the observed maximum 6.5 wt% H_2O. More complex, multistage models involving repeated episodes of differentiation of basaltic magma, or multiple stages of crustal melting, crystallization, and storage of high water contents in interstitial melt within mushy batches could also lead to the higher observed H_2O contents.

Sources of F and Cl

Even if F is completely incompatible during partial melting, crustal melts would still only reach a concentration of 1100 ppm (50 % melting; initial concentration of 557 ppm in the upper crust; Rudnick and Gao 2003). Through vapor-absent melting experiments, Skjerlie and Johnston (1992) demonstrated the possibility of forming F-rich rhyolitic melts with up to 0.31 wt% F by melting Archean tonalitic gneiss containing biotite and amphibole. We consider their experiment to be a realistic upper limit for F concentration by single-stage partial melting of the Archean crust. However, as noted above, it is physically difficult to segregate small melt fractions during crustal melting, and we consider a critical melt fraction of 30–50 % for efficient extraction of melt from the residuum (Wickham 1987). The inability to produce high F through the melting of typical or average Archean crust [even with crust containing two times the F composition reported by Rudnick and Gao (2003)] suggests other source rocks or processes (e.g., fractional crystallization) are necessary to concentrate F to such a high degree. Furthermore, a distinctive feature of the lower AVT melt inclusions is the strong enrichment of F relative to Cl (Fig. 5). Christiansen et al. (2007) suggested that the crystallization and solidification of mafic plutons in the crust could provide a mechanism to fractionate F from Cl. During plutonic solidification, F is incorporated into amphibole and/or biotite, but Cl is mostly lost to a fluid phase, creating an enriched crustal source with high F/Cl that can be later remelted.

While extreme mantle magma differentiates can in theory explain high H_2O, F, and incompatible element concentrations, 98 % differentiation and mechanical extraction of a siliceous melt is mechanically and rheologically difficult and contradicts our isotopic constraints that require substantial involvement of Archaen crust. Fractional crystallization also does not fractionate Cl from F enough to produce an order of magnitude difference in composition.

Single differentiating magma body versus multistage magma generation

We first consider a pair of single, differentiating upper crustal magma bodies (corresponding to the upper and lower AVT) formed by direct anatexis of the Archean upper crust by the heat, and using the elemental inventories added by differentiating basalt. Considering that both Nb and Rb are two of the most incompatible elements in the system, approximately 80 % fractional crystallization is required to produce the lower AVT melt inclusions from a low silica rhyolite (Fig. 8). This is greater than the 60–70 % fractional crystallization reported by Mercer et al. (2015) for the Hideaway Park Tuff topaz rhyolite. We consider 80 % fractional crystallization unrealistic because of the large volume of crystal mush that would remain in the upper crust following eruption (10^5 km^3). Volcanism at the Picabo caldera complex continued for ~4 million years after eruption of the AVT (Drew et al. 2013), and none of the subsequent eruptions share any of the unique isotopic and chemical characteristics of the AVT, making it unlikely for a large-volume residue to have remained in the crust. Additionally, a mush of this magnitude with remarkably radiogenic isotopic Archean crustal signatures would require a larger basaltic source and cumulate.

For generation of the F and incompatible trace element-enriched signature, a one-stage crystallization event would require ~98 % crystallization from basalt (starting composition of 210 ppm F; Michael and Cornell 1998), inhibiting melt extraction. Therefore, we present a model of a ramping up magmatic cycle. This multistage distillation model includes both mantle and crustal inputs, which initially mix to create isolated silicic lenses in the middle to upper crust with an enriched isotopic and trace elemental signature. Remelting of these lenses by further intrusion of basaltic differentiates, extraction of melt, fractional crystallization, and solidification of new lenses could occur in multiple stages to produce the enriched volatile, chemical, and isotopic composition of the AVT. A mass balance using batch melting and fractional crystallization calculations demonstrates that at least three stages of 50 % batch melting (of the crust and subsequent differentiates), mixing with differentiate of 25 % fractionally crystallized basalt, and solidification is required to reproduce the F, Cl, H_2O and Nb concentrations observed (Fig. 10). Additionally, up to 75 % fractional crystallization could occur in the final magma.[2]

This multistage generation mechanism (Fig. 11) would be facilitated by previous melting of the Archean crust to fractionate F and Cl and specifically create a composition enriched in F relative to Cl. Skjerlie and Johnston (1992) demonstrated that by biotite dehydration melting, fluorine-rich melt (up to 0.31 wt%) could be generated. However, the F/Cl ratio of the crust is still insufficient to fractionate F from Cl to the extent observed in the lower AVT. Therefore, repeated melting of solidified intrusions is necessary to further fractionate F from Cl. During solidification, F is largely retained in amphibole

[2] This mass balance assumes a crustal composition for F, Cl, H_2O and Nb (564 ppm, 310 ppm, 0.5 wt%, and 9 ppm, accordingly) and partition coefficients (0.2, 0.00001, 0.1, and 0.3, accordingly) and a basaltic composition (210, 80 ppm, 1 wt%, and 2.2 ppm, accordingly) and partition coefficients of 0. During solidification it is assumed that all F and Nb is retained in crystallizing phases, 10 % of the Cl and 0.5 wt% H_2O are retained and the rest is lost to the fluid phase.

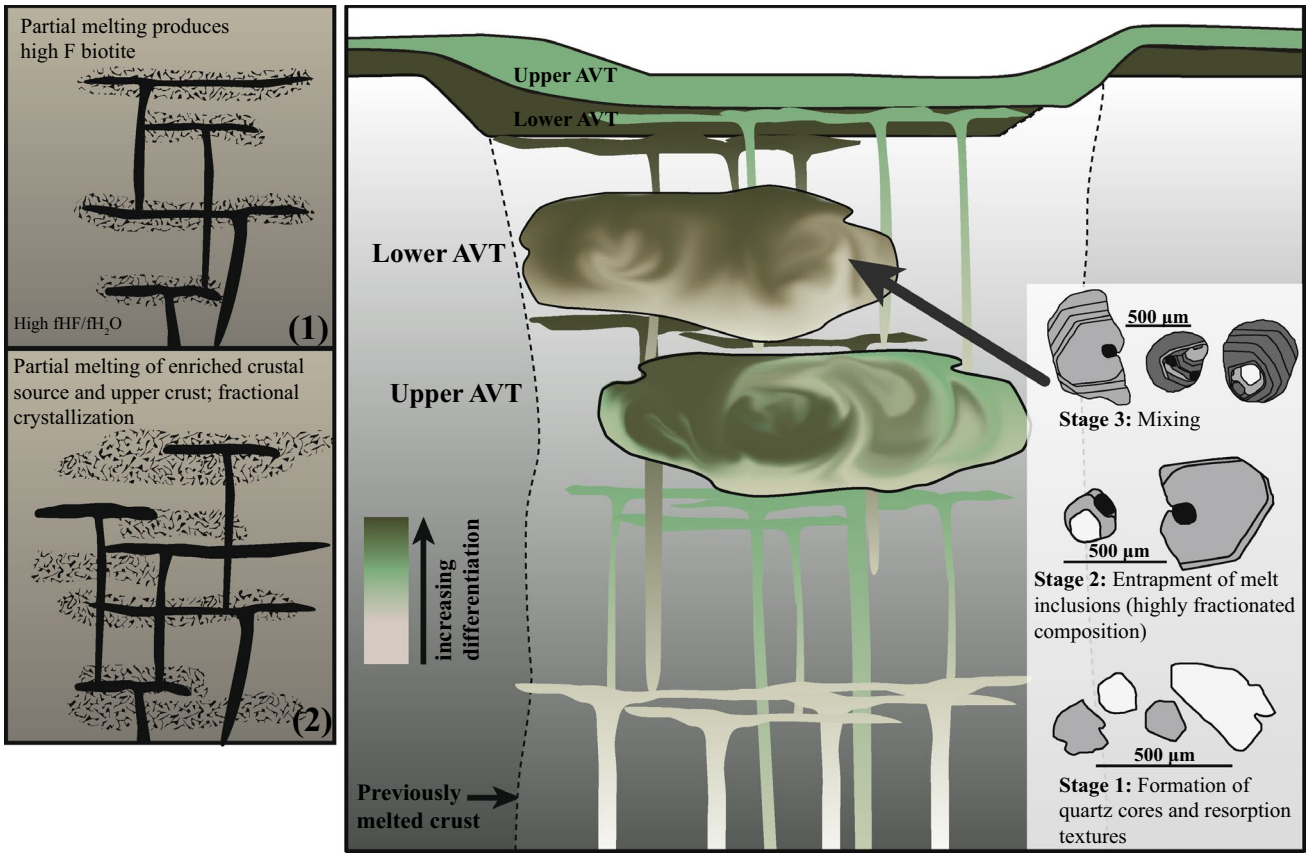

Fig. 11 Generation of the AVT magma bodies through multiple (at least three) episodes of magma injection, crystallization, solidification, and remelting. Throughout this process, a steady increase in differentiation occurs as incompatible elements are continually extracted during successive stages of remelting of differentiates leading to progressive distillation. Earlier melting of the crust provided an initial means to fractionate Cl and F. Magmatic systems of both the *upper* and *lower* AVT are shown; however, these systems could not be active contemporaneously since these units are interpreted to represent two separate eruptions. Quartz phenocrysts from the *lower* and *upper* tuff and corresponding CL zones are shown to emphasize the changes in size and Ti concentration. The *upper* AVT is generated in close spatial and temporal proximity to the *lower* AVT enabling reentrainment of quartz phenocrysts

and biotite, but Cl is mostly lost to exsolving fluids. Remelting also needs to be coupled with fractional crystallization to further enrich the extracted high F melt with other incompatible trace elements. In a sense, this model builds on the model of Christiansen et al. (2007) used to explain the formation of topaz rhyolites in the western USA.

After several episodes of partial melting of magmatic intrusions, fractional crystallization and melt extraction the melt inclusions are entrapped in the host quartz, and the quartz continues to undergo heating and breaking during magma mixing episodes, mush formation and reentrainment, and/or convective circulation in a magma body to produce the observed CL patterns. Unlike subsequent rhyolites in the Picabo volcanic field that are related to recycling of intracaldera tuffs in caldera complexes and have low-$\delta^{18}O$ signatures, we envision that the formation of the AVT and other chemically similar rhyolites formed during the initiation of individual caldera clusters (Fig. 11) and involve prolonged, mid-crustal, low-melt production intrusion and differentiation episodes.

Concluding remarks and implications for the initiation of caldera complexes in the SRP

The Yellowstone hotspot track has produced an abundance of hot, dry, and densely welded silicic volcanic rocks preserved as caldera clusters in the eastern SRP, but occasional more hydrous and lower-temperature eruptive units from the initial eruptions at individual caldera clusters have been produced as well. The AVT and first-order chemical and isotopic similarities to the Jarbidge Rhyolite, Huckleberry Ridge Tuff-Member C, and Blacktail Creek Tuff demonstrate that these initial eruptions provide additional insight into rhyolite generation during caldera cluster initiation. These units herald the early ramping up stage of caldera cluster volcanism with greater crustal contribution and lower mantle plume output. Typically, these eruptive products can be poorly exposed due to burial by subsequent volcanic activity, and since their plutonic equivalents were likely cannibalized by subsequent crustal melting during

repeated caldera-forming eruptions. However, in this study pumice clasts from the fallout tuff of the AVT were preserved providing the opportunity to study the geochemistry of glassy quartz-hosted rhyolitic melt inclusions in the context of isotopic constraints.

The major element chemistry of the upper and lower AVT melt inclusions, trace element geochemistry of the interstitial glass and whole-rock, O and Sr isotopic differences and temperature differences determined from Ti in quartz and $\Delta^{18}O$(Qz-Mt) demonstrate that the upper and lower AVT represent two separate eruptions, temporally or spatially separated. This conclusion is in agreement with the $^{40}Ar/^{39}Ar$ populations observed for the lower and upper AVT by Anders et al. (2014) (10.41 and 10.22 Ma, respectively). The large range in Ti concentrations of the upper AVT and overlapping isotopic and trace element characteristics with the lower AVT suggest possible reentrainment of lower AVT residuum during evolution of the upper AVT magma.

Chemical data from rhyolitic melt inclusions in the framework of CL imaging and Ti measurements of the host quartz from the fallout of the AVT coupled with isotopic constraints elucidate the mechanism by which lower-temperature, high-H_2O (up to 6.4 wt%), high-F (up to 1.38 wt%), and incompatible element-rich rhyolites can be generated in the SRP. For generation of the high-F/Cl and trace element-enriched signature of the lower AVT, we present a model of a ramping up magmatic cycle because a one-stage crystallization event would require greater than 90 % crystallization, inhibiting melt extraction. This distillation model includes both mantle and crustal inputs, which initially mix to create enriched isotopic and trace elemental signatures in the middle to upper crust forming isolated silicic lenses. Repeated rejuvenation and differentiation coupled with remelting of solidified magmatic intrusions leads to multistage remelting/crystallization of already sequestered silicic melt bodies emplaced in the crust to produce the enriched volatile and chemical composition of the AVT.

This study emphasizes that the lower AVT is similar to topaz rhyolites and highly radiogenic and/or high H_2O rhyolites in the SRP, such as the Jarbidge Rhyolite, Huckleberry Ridge Tuff-Member C, and Blacktail Creek Tuff. The AVT is generated by an increasing magma influx from the onset of plume impingement followed by multi-stage fractional crystallization, crustal melting, and melting of solidified magma injections (at degrees greater than 30–50 %), occurring in the middle to upper crust without intracaldera rhyolite recycling and formation of low-$\delta^{18}O$ signatures. First-order similarities of the AVT to the other units representing caldera cluster initiation at a new location demonstrate that this model for generating the AVT has implications for caldera cluster initiation throughout the SRP.

Acknowledgments The authors gratefully acknowledge Madison Myers, Kristina Walowski, Robin Tuohy, and James Rea for all of their help in learning to prepare doubly polished melt inclusions and for their analytical help. We also thank Jim Palandri, John Donovan, Julie Chouinard, and Adam Kent for their analytical help as well. We thank Michael McCurry and Dylan Colón for fieldwork assistance, and Angela Seligman for helpful discussions. We also appreciate the constructive reviews by Eric Christiansen and Guil Gualda that greatly helped us to improve the final manuscript. This work was supported by NSF Grant EAR/CAREER-844772.

References

Agangi A, Kamenetsky VS, McPhie J (2012) Evolution and emplacement of high fluorine rhyolites in the Mesoproterozoic Gawler silicic large igneous province, South Australia. Precam Res 208–211:124–144

Almeev R, Bolte T, Nash B, Holtz F, Erdmann M, Cathey H (2012) High-temperature, low-H_2O Silicic Magmas of the Yellowstone Hotspot: an Experimental Study of Rhyolite from the Bruneau–Jarbidge Eruptive Center, Central Snake River Plain, USA. J Petrol 53(9):1837–1866

Anders M, Saltzman J, Hemming S (2009) Neogene tephra correlations in eastern Idaho and Wyoming; Implications for Yellowstone hotspot-related volcanism and tectonic activity. Geol Soc Am Bull 121(5–6):837–856

Anders MH, Rodgers DW, Hemming SR, Saltzman J, DiVenere VJ, Hagstrum JT, Embree GF, Walter RC (2014) A fixed sublithospheric source for the late Neogene track of the Yellowstone hotspot: implications of the Heise and Picabo volcanic fields. J Geophys Res Solid Earth 119:2871–2906

Anderson AT, Davis AM, Fangqiong L (2000) Evolution of Bishop Tuff rhyolitic magma based on melt and magnetite inclusions and zoned phenocrysts. J Petrol 41(3):449–473

Armstrong RL (1978) Cenozoic igneous history of the U.S. Cordillera from latitude 42° N to 49° N. Geol Soc Am Mem 152:265–282

Bacon CR, Newman S, Stolper E (1992) Water, CO_2, Cl, and F in melt inclusions in phenocrysts from three Holocene explosive eruptions, Crater Lake, Oregon. Am Mineral 77:1021–1030

Bindeman IN (2005) Fragmentation phenomena in populations of magmatic crystals. Am Mineral 90:1801–1815

Bindeman IN, Valley JW (2002) Oxygen isotope study of the Long Valley-Glass Mountain magmatic system, California: isotope thermometry and convection in large silicic magma bodies. Contrib Mineral Petrol 144:185–205

Bindeman IN, Watts KE, Schmitt AK, Morgan LA, Shanks PWC (2007) Voluminous low-$\delta^{18}O$ magmas in the late Miocene Heise volcanic field, Idaho: implications for the fate of Yellowstone hotspot calderas. Geology 35:1019–1022

Bindeman IN (2008) Oxygen isotopes in mantle and crustal magmas as revealed by single crystal analysis. In: Putirka KD, Tepley FJ III (eds) Minerals, inclusions and volcanic processes. Mineralogical Society of America and Geochemical Society, Reviews in Mineralogy and Geochemistry 69:445–478

Bonnichsen B, Leeman WP, Honjo N, McIntosh WC, Godchaux MM (2008) Miocene silicic volcanism in southwestern Idaho: geochronology, geochemistry, and evolution of the central Snake River Plain. Bull Volcan 70:315–342

Boroughs S, Wolff JA, Bonnichsen B, Godchaux M, Larson PB (2005) Large-volume, low-$\delta^{18}O$ rhyolites of the central Snake River Plain, Idaho, USA. Geology 33:821–824

Boroughs S, Wolff JA, Ellis BS, Bonnichsen B, Larson PB (2012) Evaluation of models for the origin of Miocene low-$\delta^{18}O$

rhyolites of the Yellowstone/Columbia River Large Igneous Province. Earth Planet Sci Lett 313–213:45–55

Branney MJ, Bonnichsen B, Andrews GDM, Ellis B, Barry TL, McCurry M (2008) "Snake River (SR)-type" volcanism at the Yellowstone hotspot track: distinctive products from unusual, high-temperature silicic super-eruptions. Bull Volcan 70(3):293–314

Brueseke ME, Callicoat JS, Hames W, Larson PB (2014) Mid-Miocene rhyolite volcanism in northeastern Nevada: the Jarbidge Rhyolite and its relationship to the Cenozoic evolution of the northern Great Basin (USA). GSA Bull 126(7/8):1047–1067

Burt DM, Sheridan MF, Bikun JV, Christiansen EH (1982) Topaz rhyolites-distribution, origin, and significance for exploration. Econ Geol 77:1818–1836

Cathey HE, Nash BP (2004) The Couger Point tuff: implications for thermochemical zonation and longevity of high-temperature, large-volume silicic magmas of the Miocene Yellowstone Hotspot. J Petrol 45(1):27–58

Cathey HE, Nash BP, Allen CM, Campbell IH, Valley JW, Kita N (2008) U-Pb zircon geochronology and Ti-in-zircon thermometry of large-volume low-δ18O magmas of the Miocene Yellowstone hotspot. Geochim Cosmochim Acta 72:A143

Chamberlain KJ, Wilson CJN, Wallace PJ, Millet MA (2015) Micro-analytical perspectives on the Bishop Tuff and its magma chamber. J Petrol 56(3):605–640

Chiba H, Chacko T, Clayton RN, Goldsmith JR (1989) Oxygen isotope fractionations involving diopside, forsterite, magnetite, and calcite—application to geothermometry. Geochim Cosmochim Acta 53:2985–2995

Christiansen EH (2005) Contrasting processes in silicic magma chambers: evidence from very large volume ignimbrites. Geol Mag 142(6):669–681

Christiansen EH, McCurry M (2008) Contrasting origins of Cenozoic silicic volcanic rocks from the western Cordillera of the United States. Bull Volcan 70:251–267

Christiansen E, Burt D, Sheridan M, Wilson R (1984) The petrogenesis of topaz rhyolites from the western United States. Contrib Mineral Petrol 83(1–2):16–30

Christiansen E, Sheridan M, Burt D (1986) The geology and geochemistry of Cenozoic topaz rhyolites from the western United States. GSA Special Paper 205, 82 pp

Christiansen EH, Haapala I, Hart GL (2007) Are Cenozoic topaz rhyolites the erupted equivalents of Proterozoic rapakivi granite? Examples from the western United States and Finland. Lithos 97:219–246

Clemens JD (1990) The granulite-granite connection. In: Vielzeuf D, Vidal P (eds) Granilites and Crustal Evolution :25–36

Colón D, Bindeman I, Stern R, Fisher C (2015a) How do mantle plumes shape the continental crust: evidence from isotopically diverse rhyolites coeval with the Columbia River Flood Basalts. Terra Nova 27(4):270–276

Colón DP, Bindeman IN, Schmitt AK, Fisher CM (2015b) Hydrothermal alteration and melting of the crust during the Columbia River Basalt eruptions: evidence from coeval rhyolites in southwest Idaho and northern Nevada. Lithos 224–225:310–323

Drew DL, Bindeman IN, Watts KE, Schmitt AK, Fu B, McCurry M (2013) Crustal-scale recycling in caldera complexes and rift zones along the Yellowstone hotspot track: O and Hf isotopic evidence in diverse zircons from voluminous rhyolites of the Picabo volcanic field, Idaho. Earth Planet Sci Lett 381:63–77

Dufek J, Bachman O (2010) Quantum magmatism: magmatic compositional gaps generated by melt-crystal dynamics. Geology 38:687–690

Ellis BS, Barry T, Branney MJ, Wolff JA, Bindeman IN, Wilson R, Bonnichsen B (2010) Petrologic constraints on the development of a large-volume, high temperature, silicic magma system: the Twin Falls eruptive center, central Snake River Plain. Lithos 120:475–489

Ellis BS, Wolff JA, Boroughs S, Mark DF, Starkel WA, Bonnichsen B (2013) Rhyolitic volcanism of the central Snake River Plain: a review. Bull Volcanol 75:745

Gansecki CA (1998) $^{40}Ar/^{39}Ar$ geochronology and pre-eruptive geochemistry of the Yellowstone Plateau volcanic field rhyolites. Stanford University Ph.D. thesis

Glazner AF, Coleman DS, Bartley JM (2008) The tenuous connection between high-silica rhyolites and granodiorite plutons. Geology 36(2):182–186

Gualda GAR, Ghiorso MS (2013) The Bishop Tuff giant magma body: an alternative to the Standard Model. Contrib Mineral Petrol 166:755–775

Hildreth EW (1977) The magma chamber of the Bishop Tuff; gradients in temperature, pressure, and composition. Ph.D. thesis University of California at Berkeley, pp 1–328

Hildreth W (1979) The Bishop Tuff: evidence for the origin of compositional zonation in silicic magma chambers. Geol Soc Am Spec Pap 180:43–75

Hildreth W, Wilson CJN (2007) Compositional zoning of the Bishop Tuff. J Petrol 28(5):951–999

Hildreth W, Christiansen RL, O'Neil JR (1984) Catastrophic isotopic modification of rhyolitic magma at times of caldera subsidence, Yellowstone Plateau volcanic field. J Geophys Res 89(B10):8339–8369

Hildreth W, Halliday AN, Christiansen RL (1991) Isotopic and chemical evidence concerning the genesis and contamination of basaltic and rhyolitic magmas beneath the Yellowstone Plateau volcanic field. J Petrol 32:63–138

Honjo N (1990) Geology and stratigraphy of the Mount Bennett Hills, and the origin of west-central Snake River Plain rhyolites. Ph.D. thesis, Rice University 1–259

Huang R, Audetat A (2012) The titanium-in-quartz (TitaniQ) thermobarometer: a critical examination and re-calibration. Geochim Cosmochim Acta 84:75–89

Jezek PA, Noble DC (1978) Natural hydration and ion exchange of obsidian: an electron microprobe study. Am Miner 63:266–273

John DA, Wallace AR, Ponce DA, Fleck RB, Conrad JE (2000) New perspectives on the geology and origin of the northern Nevada Rift. In: Cluer JK, Price JG, Struhsacker EM, Hardyman RF, Morris CL (eds) Geology and ore deposits 2000: the great basin and beyond: geological society of Nevada symposium proceedings, May 15–18, pp 127–154

Kellogg KS, Harlan SS, Mehnert HH, Snee LW, Pierce KL, Hackett WR, Rodgers DW (1994) Major 10.2 Ma rhyolitic volcanism in the eastern Snake River Plain, idaho-isotopic age and stratigraphic setting of the Arbon Valley Tuff Member of the Starlight Formation. US Geol Surv Bull 2091:1–18

Konstantinou A, Strickland A, Miller EL, Wooden JP (2012) Multistage Cenozoic extension of the Albion–Raft River–Grouse Creek metamorphic core complex: geochronologic and stratigraphic constraints. Geosphere 8(6):1–38

Loewen MW, Kent AJR (2012) Sources of elemental fractionation and uncertainty during the analysis of semi-volatile metals in silicate glasses using LA-ICP-MS. J Anal At Spectrom 27:1502–1508. doi:10.1039/c2ja30075c

Lukkari S, Thomas R, Haapala I (2009) Crystallization of the Kymi topaz granite stock within the Wiborg rapakivi granite batholith, Finland: evidence from melt inclusions. Can Mineral 47:1359–1374

McCurry M (2009) The Arbon Valley Tuff: a new look at a highly anomalous ignimbrite from the Yellowstone-Snake River Plain volcanic track. Geol Soc Am Abstr Progr 41(6):43

McDonough WF, Sun SS (1995) The composition of the Earth. Chem Geol 120:223–253

Mercer CN, Hofstra AH, Todorov TI, Roberge J, Burgisser A, Adams DT, Cosca M (2015) Topaz rhyolite: insights into metal source and evolution of magma parental to the Henderson porphyry molybdenum deposit, Colorado. J Petrol 56(4):645–679

Michael PJ, Cornell WC (1998) Influence of spreading rate and magma supply on crystallization and assimilation beneath mid-ocean ridges: evidence from chlorine and major element chemistry of mid-ocean ridge basalts. J Geophys Res 103:8325–18356

Nash B, Perkins M, Christensen J, Lee D, Halliday A (2006) The Yellowstone hotspot in space and time: Nd and Hf isotopes in silicic magmas. Earth Planet Sci Lett 247(1–2):143–156

Newman S, Lowenstern JB (2002) VolatileCalc: a silicate melt-H_2O–CO_2 solution model written in Visual Basic for excel. Comput Geosci 28:597–604

Patiño Douce AE, Beard JS (1995) Dehydration melting of biotite gneiss and quartz amphibolite from 3 to 15 kbar. J Petrol 96:707–738

Peccerillo A, Taylor SR (1976) Geochemistry of Eocene calc-alkaline volcanic rocks of the Kastamonu area, northern Turkey. Contrib Mineral Petrol 58:63–81

Roberge J, Wallace PJ, Kent ARJ (2013) Magmatic processes in the Bishop Tuff rhyolitic magma based on trace elements in melt inclusions and pumice matrix glass. Contrib Mineral Petrol 165:237–257

Rudnick RL, Gao S (2003) Composition of the continental crust. In: Rudnick RL (ed) The crust vol 3, Treatise on geochemistry

Seligman AN, Bindeman IN, McClaughry J, Stern RA, Fisher C (2014) The earliest low and high δ18O calderaformingeruptions of the Yellowstone plume: implications for the 30–40 Ma Oregon calderas and speculations onplume-triggered delaminations. Front Earth Sci 28:1–9

Severs MJ, Azbej T, Thomas JB, Mandeville JB, Bodnar RJ (2007) Experimental determination of H_2O loss from melt inclusions during laboratory heating: evidence from Raman spectroscopy. Chem Geol 237:358–371

Simakin AG, Bindeman IN (2012) Remelting in caldera and rift environments and the genesis of hot, "recycled" rhyolites. Earth Planet Sci Lett 337–338:224–235

Skjerlie KP, Johnston DA (1992) Vapor-absent melting at 10 kbar of a biotite- and amphibole-bearing tonalitic gneiss: implications for the generation of A-type granites. Geology 20:263–266

Stefano CJ, Mukasa SB, Andronikov A, Leeman WP (2011) Water and other volatile systematics of olivine-hosted melt inclusions from the Yellowstone hotspot track. Contrib Mineral Petrol 161:615–633

Stewart JH, Walker GW, Kleinhampl FJ (1975) Oregon-Nevada lineament. Geology 3:265–268

Sun SS, McDonough WF (1989) Chemical and isotopic systematics of oceanic basalts: implications for mantle composition and processes. In: Saunders AD, Norry MJ (eds) Magmatism in the ocean basins. Geol Soc Special Publication 42:313–345

Suneson NH, Lucchitta I (1983) Origin of bimodal volcanism, southern Basin and Range province, west-central Arizona. Geol Soc Am Bull 94:1005–1019

Szymanowski D, Ellis BS, Bachmann O, Guillong M, Phillips WM (2015) Bridging basalts and rhyolites in the Yellowstone-Snake River Plain volcanic province: the elusive intermediate step. Earth Planet Sci Lett 415:80–89

Thomas JB, Watson EB, Spear FS, Shemella FS, Nayak SK, Lanzinotti A (2010) TitaniQ under pressure: the effect of pressure and temperature on the solubility of Ti in quartz. Contrib Mineral Petrol 160:743–759

Thomas JB, Watson EB, Spear FS, Wark DA (2015) TitaniQ recrystallized: experimental confirmation of the original Ti-in-quartz calibrations. Contrib Mineral Petrol 169(27):1–16

Thompson AB (1982) Dehydration melting of pelicitc rocks and the generation of H_2O-undersaturated granitic liquids. Am Mus Sci 282:1567–1595

Trimble DE, Carr WJ (1976) Geology of the Rockland and Arbon Quadrangles, Power County, Idaho. Geol Surv Bull 1399:1–115

Vazquez JA, Manning CE, Reid MR (2004) Experimental determination of allanite stability in high-silica rhyolite. American Geophysical Union abstracts V41C-1407

Wallace PJ (2005) Volatiles in subduction zone magmas: concentrations and fluxes based on melt inclusion and volcanic gas data. J Volcan Geotherm Res 140:217–240

Wallace PJ, Anderson AT, Davis AM (1999) Gradients in H_2O, CO_2, and exsolved gas in a large-volume silicic magma system: interpreting the record preserved in melt inclusions from the Bishop Tuff. J Geophys Res 104(B9):20097–20122

Wark DA, Hildreth W, Spear FS, Cherniak DJ, Watson EB (2007) Pre-eruption recharge of the Bishop magma system. Geology 35:235–238

Wark D, Watson E (2006) TitaniQ: a titanium-in-quartz geothermometer. Contrib Mineral Petrol 152(6):743–754

Watts KE, Bindeman IN, Schmitt AK (2011) Large-volume rhyolite genesis in caldera complexes of the Snake River Plain: insights from the Kilgore Tuff of the Heise Volcanic Field, Idaho, with comparison to Yellowstone and Bruneau–Jarbidge Rhyolites. J Petrol 52(5):857–890

Watts KE, Bindeman IN, Schmitt AK (2012) Crystal scale anatomy of a dying supervolcano: an isotope and geochronology study of individual phenocrysts from voluminous rhyolites of the Yellowstone caldera. Contrib Mineral Petrol 164(1):45–67

Wegert D, Parker D, Ren M (2013) The Nathrop Domes, Colorado: geochemistry and petrogenesis of a topaz rhyolite. Rocky Mt Geol 48(1):1–14

Wickham SM (1987) The segregation and emplacement of granitic magmas. J Geol Soc 144:281–297

Williams H (1941) Calderas and their origin. Bull Dept Geol Sci, 25 Univ of California Press Berkeley: 239–346

Wilson CJN, Seward TM, Allan ASR, Charlier BLA, Bello L (2012) A comment on: 'TitaniQ under pressure: the effect of pressure and temperature on the solubility of Ti in quartz', by Jay B. Thomas, E. Bruce Watson, Frank S. Spear, Philip T. Shemella, Saroj K. Nayak and Antonio Lazirotti. Conrib Mineral Petrol 164:359–368

Wright HM, Bacon CR, Vazquez JA, Sisson TW (2012) Sixty thousand years of magmatic volatile history before the caldera-forming eruption of Mount Mazama, Crater Lake, Oregon. Contrib Mineral Petrol 164:1027–1052

Zhang Y, Belcher R, Ihinger PD, Wang L, Xu Z, Newman S (1997) New calibration of infrared measurement of dissolved water in rhyolitic glasses. Geochim Cosmochim Act 61(15):3089–3100

Zoback ML, Thompson GA (1978) Basin and Range rifting in northern Nevada—clues from a mid-Miocene rift and its subsequent offsets. Geology 6:111–116

Zoback ML, Anderson RE, Thompson GA (1981) Cenozoic evolution of the state of stress and style of tectonism of the Basin and Range province of the western United States. R Soc Lond Philos Trans 300:407–434